DEVELOPMENT OF FIBER-BASED FLUORESCENCE IMAGING TO STUDY BACTERIAL INFECTION

A Dissertation

by

FATEMEH NOOSHABADI

Submitted to the Office of Graduate and Professional Studies of
Texas A&M University
in partial fulfillment of the requirements for the degree of

DOCTOR OF PHILOSOPHY

Chair of Committee,	Kristen C. Maitland
Committee Members,	Jeffrey D. Cirillo
	Brian E. Applegate
	Gerard L. Coté
Head of Department,	Anthony Guiseppi-Elie

August 2016

Major Subject: Biomedical Engineering

ABSTRACT

Tuberculosis (TB) is a deadly pulmonary disease with an especially high mortality rate in immuno-compromised populations, specifically children and HIV positive individuals. The causative agent, *Mycobacterium tuberculosis* (Mtb), is very slow growing—making both diagnosis and development of effective treatments very difficult. Whole-animal fluorescence imaging with recombinant or fluorescently-tagged pathogens or cells enables real time analysis of disease progression and treatment response in live animals. However, tissue absorption limits penetration of fluorescence excitation light, particularly in the visible wavelength range, resulting in reduced sensitivity to deep targets. In this dissertation, the use of an optical fiber bundle to deliver light into the mouse lung to excite fluorescent bacteria was shown to circumvent tissue absorption of excitation light in a whole-animal imaging system. A fiber-optic fluorescence microendoscope was integrated into a whole-body imaging system for in-vivo Mtb detection.

First, we employed this technology to improve detection of recombinant reporter strains of tdTomato-expressing *Mycobacterium bovis* BCG (Bacillus Calmette Guerin) bacteria in the mouse lung. Using this technique, the threshold of detection was measured as 10^3 colony forming units (CFU) during pulmonary infection. In comparison, the threshold of detection for whole-animal fluorescence imaging using standard epi-illumination was greater than 10^6 CFU.

We next exploited an endogenous enzyme of Mtb (β-lactamase, or BlaC) using a BlaC-specific NIR fluorogenic substrate. In the presence of BlaC, this substrate is cleaved and becomes fluorescent. Using intravital illumination of the lung with the fiber

microendoscope to excite this probe, the sensitivity of the optical system increases over trans-illumination and epi-illumination methods of whole-body fluorescence imaging. We demonstrated that the integration of these optical imaging technologies with a BlaC-specific fluorescent reporter probe increases the system sensitivity by two orders of magnitude, allowing detection down to ~100 colony forming unit (CFU) infection. This lower detection threshold enables the study of early stage bacterial infection and could allow for longitudinal studies of disease pathogenesis and therapeutic efficacy with multiple time points measured in a single animal.

DEDICATION

To my loving parents, kind siblings, and my amazing husband

To my beloved grandparents

ACKNOWLEDGEMENTS

I would like to express my special appreciation and thanks to my committee chair and advisor, Dr. Kristen Maitland for all her help, support, understanding and guidance throughout my study. You have been a tremendous mentor for me. I would like to thank you for encouraging my research and for allowing me to grow as a research engineer. Your advice on both research as well as on my career have been priceless.

I would also like to thank my committee members, Dr. Cirillo, Dr. Coté, and Dr. Applegate for their guidance and support throughout the course of this research.

Thanks also to my friends and colleagues and staff in the Biomedical Engineering department for being there to support when I needed.

Thanks to Dr. Hee-jeong Yang, Madeleine Durkee, Taylor Hinsdale, Joel Bixler, Cory Olsovsky, Meagan Harris, Joey Jabbour, and Dr. Bilal Malik for their helps and support during the past five years.

Finally, thanks to my kind mother, father, brother and sister for their encouragement, who without their support I could not accomplish this. Also special thanks to my wonderful, amazing husband; I am truly grateful for your love, support, and patience. Without you, I would not have been able to thrive in my doctoral program or balance my research with everything else. Thanks for joining me in this scholarly adventure.

NOMENCLATURE

AFB	Acid-fast Bacilli
AMs	Alveolar Macrophages (AMs)
BCG	Bacille Calmette Guérin
BPI	Biophotonic Imaging
CFP-10	Culture Filtrate Protein-10
Cy5	Cynine-5
DTH	Delayed-type Hypersensitivity
ELISA	Enzyme-Linked Immunosorbent Assay
ELISPOT	Enzyme Linked Immunospot
ESAT-6	Early Secretory Antigenic Target-6
FDA	Food and Drug Administration
FOB	Fiber Optic Biosensors
FPs	Fluorescent Proteins
GFP	Green Fluorescent Protein
HIV	Human Immunodeficiency Virus
IFN-γ	Interferon-gamma
i.p.	Intraperitoneal
i.v.	Intravenous
LTBI	Latent TB Infection
Mtb	*Mycobacterium tuberculosis*

NIR	Near Infra-Red
PPD	Protein-purified Derivative
RD-1	Region of Difference-1
REF	Reporter Enzyme Fluorescence
TB	Tuberculosis
TST	Tuberculin skin test
WHO	World Health Organization

TABLE OF CONTENTS

Page

LIST OF FIGURES

Page

LIST OF TABLES

Page

CHAPTER I

INTRODUCTION

The ultimate goal of all the experiments in this dissertation is to develop a new imaging technique for localized high-resolution imaging and simultaneous intravital fluorescence excitation in whole-animal imaging to improve the level of detection of bacteria – Tuberculosis (TB) - in live animals. The two main projects contained in this dissertation can be split into two aims: 1) whole-animal imaging of recombinant strains of bacteria using an intravital illumination source to enhance the detection threshold of standard whole-animal imaging systems; and 2) the combination of the developed imaging technique with reporter enzyme fluorescence (REF) technology to enable whole-body imaging that does not require recombinant strains in an effort to facilitate potential translation to clinical pediatric applications.

Chapter II, covers the background on TB disease and the optical techniques for TB detection. In chapter III, the importance of using animal models for bacterial detection and the different techniques for animal's infection is presented. Chapter IV demonstrates the optical system design for fiber-optic microendoscope and the diffusing fiber, as well as the integration of the fiber-optic microendoscope into the whole-animal imaging system. The results for preliminary experiment are also presented in chapter IV. In chapter V, we employ the intravital illumination microendoscope integrated to the whole-animal imager for detection of recombinant reporter strains of tdTomato-expressing *Mycobacterium bovis* BCG bacteria in the mouse lung. In chapter VI, the integrated imaging system in

combined with a BlaC-specific NIR fluorogenic substrate and REF technology is used to improve the detection sensitivity of the developed imaging technique. Chapter VII summarizes the major contribution of this dissertation, as well as the future work.

CHAPTER II

OPTICAL DETECTION OF TUBERCULOSIS

2.1 Tuberculosis infection

Infectious diseases are the most common cause of death in humans worldwide, especially in developing countries. It has been reported that 95% of reported cases of infectious diseases occur in low income countries, where infectious disease accounts for over half of all neonatal deaths [1].

Tuberculosis (TB) remains a major global health problem, infecting one third of the world's population based on World Health Organization (WHO) estimations [1]. Although TB disease seems to be more common in developing countries, it is also a major problem in industrialized countries. High rate of immigration, rapid increase in poverty, poor nutrition, war, and limited access to proper medication are the most important factors leading to revival of TB in these countries [2].

TB, caused by an acid-fast bacillus *Mycobacterium tuberculosis* (Mtb), is transmitted via the respiratory route. Infection primarily occurs in the lungs, but it can also affect organs in the central nervous system, lymphatic system, and circulatory system among others via hematogenous spread. The bacteria in the lungs multiply and cause pneumonia along with chest pain, coughing up blood, and a prolonged cough. In addition, lymph nodes near the heart and lungs become enlarged. As the TB tries to spread to other parts of the body, it is often interrupted by the body's immune system. If the body's immune system is unable to fight TB (HIV infected people), the disease returns to an

active state with pneumonia and damage to kidneys, bones, and the meninges that line the spinal cord and brain [3, 4]. This risk is increased by 20-30 times if co-infected with HIV [1].

TB is a major cause of illness and death worldwide, especially in Asia (56%) and Africa (29%). As show in Figure 1, in 2013, there were an estimated 9 million incident cases of TB (range, 8.6 million-9.4 million) globally, equivalent to 126 cases per 100,000 population. Also, there were an estimated 1.5 million TB death in 2013, which were about 1.1 million among HIV-negative people and 360,000 among HIV-positive people. TB is second only to HIV/AIDS as the greatest killer worldwide due to a single infectious agent and is the leading killer of people living with HIV [1, 3].

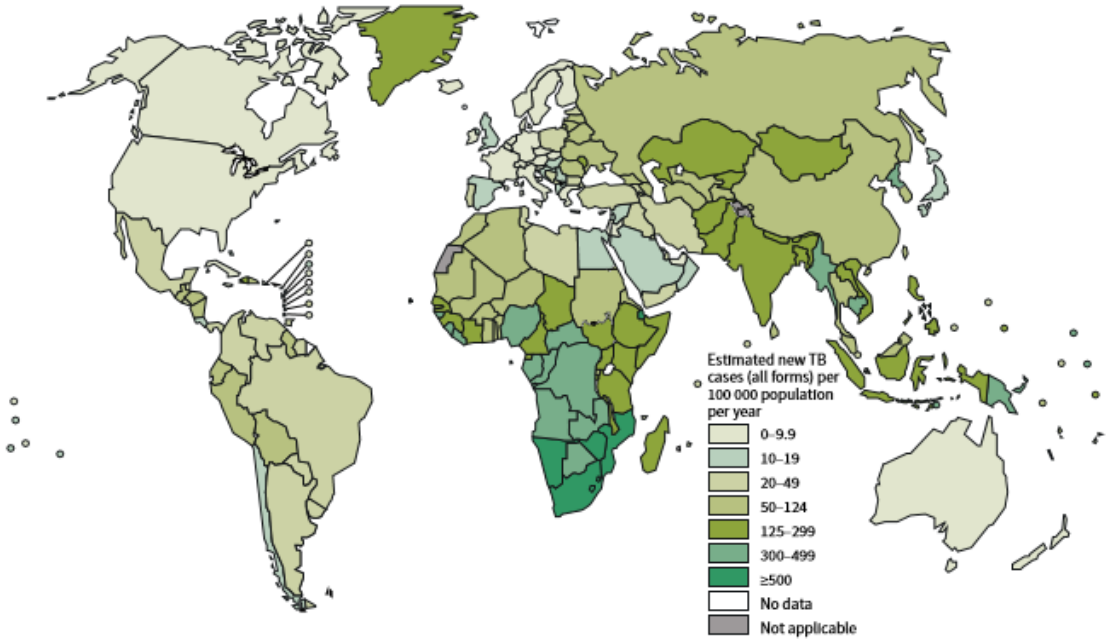

Figure 1: Estimated TB incidence rate, 2013 [1]

TB germs are spread person to person through the air when a person with untreated pulmonary TB coughs, sneezes, laughs, and sings. However, it is not spread by sharing silverware or cups, sharing cigarettes, or sharing saliva when kissing someone. Prolonged exposure to a person with untreated TB usually is necessary for infection to occur. Anyone can get tuberculosis, but certain factors can increase your risk of the disease, such as: people with weakened immune system (HIV/AIDS, diabetes, end-stage kidney disease, etc.), people who are travelling or are living or have been born in a high risk area (sub-saharan Africa, India, China, Russia, Pakistan), poverty and substance abuse (lack of medical care, substance abuse, tobacco use), and regular contact with people who are ill (family members, friends, coworkers, nurses) [1, 3].

Mtb is mainly considered an airborne pathogen. One of the possible outcomes for a person encountering Mtb is that the bacillus can be immediately destroyed by the host's innate responses. The other possibility is that the person who is infected with Mtb develops active TB within a time frame of 1 to 3 years. This group of people are unable to develop a protective response in time to prevent the disease. The final possible outcome is that a majority of people infected with Mtb have a clinically latent infection. This group of people show positive purified protein derivative (PPD) by skin test, but they do not show any clinical symptoms of TB and are not contagious to others. However, In approximately 5 to 10% of latently infected persons, the infection will reactivate and cause active tuberculosis [4, 5].

The infection process can be divided into three stages. First, aerosol droplets containing Mtb are transmitted from an infected individual to a healthy person. Once Mtb

enters the lungs, it resides within alveolar macrophages (AMs) and dendritic cells. In the primary infection, Mtb replicates within the macrophage and induces cytokines that initiate the mild inflammatory response in the lungs. Second, AMs and lymphocytes migrate to the site of infection and form cell-mediated immunity and granulomas, where macrophages become activated to kill intracellular Mtb. Granulomas are responsible to segregate the infection to prevent spread to the other parts of the lung and to other organs, as well as concentrate the immune response at the site of infection. At this stage more than 90% of infected people remain asymptomatic, and live bacilli have been isolated from granulomas or tubercles in the lungs of persons with clinically inactive tuberculosis. Finally, when latent TB is reactivated and causes active disease, either because of a decline in the host's immunity or a failure to develop and maintain immune signals [4, 6].

Although TB treatment has been successful over the past 25 years using a six-month course of antimicrobial drugs, multi-drug resistant strains of Mtb remain a significant challenge to the development of effective new antimicrobial therapies [7, 8]. In addition, the efficiency of *Mycobacterium bovis* Bacillus Calmette Guérin (BCG), which is the current vaccine to prevent TB infections worldwide, is variable depending upon the population being vaccinated, from 0-80% [9, 10]. Early diagnosis and proper treatment of TB could reduce the rate of TB transmission worldwide and decrease the risk of latent TB infection (LTBI) to become active.

2.2 TB diagnosis techniques

In order to improve the sensitivity and specificity of methods for TB detection, there is a growing need for more accurate and rapid diagnostic techniques. Currently, there are several diagnostic tests that are used to determine if a person has been infected with TB bacteria: the Tuberculin skin test (TST), TB blood tests, sputum smear microscopy, sputum culture, and chest x-ray.

TST or intradermal Mantoux is the oldest diagnostic test and has been used for TB infection since 1910. It is more widely used in countries with low rates of TB to test for LTBI. Although TST has poor specificity in BCG-vaccinated persons, low sensitivity in people with weakened cellular immunity (young children, HIV infected patients), and several logistic drawbacks, it is still included in the WHO latest recommendations for TB control. TST is performed by injecting 0.1 ml of tuberculin protein–purified derivative (PPD) into the inner surface of the lower part of the arm, which forms a culture filtrate of tubercle bacilli containing over 200 antigens common both in BCG vaccine and in most non tuberculosis bacteria. In other words, TST uses the fact that LTBI produces a strong cell-mediated immune response by measuring the delayed-type hypersensitivity (DTH) response to intradermal inoculation of tuberculin PPD after 48-72 hours of the initial administration (Figure 2, left). In addition to errors of TST placement and reading, TST can produce both false positive (anamnestic immune reaction) and false negative (severe active TB or immunosuppressed patients) results. Therefore, TST test has low specificity and is not very powerful in diagnosis of LTBI [2, 11, 12].

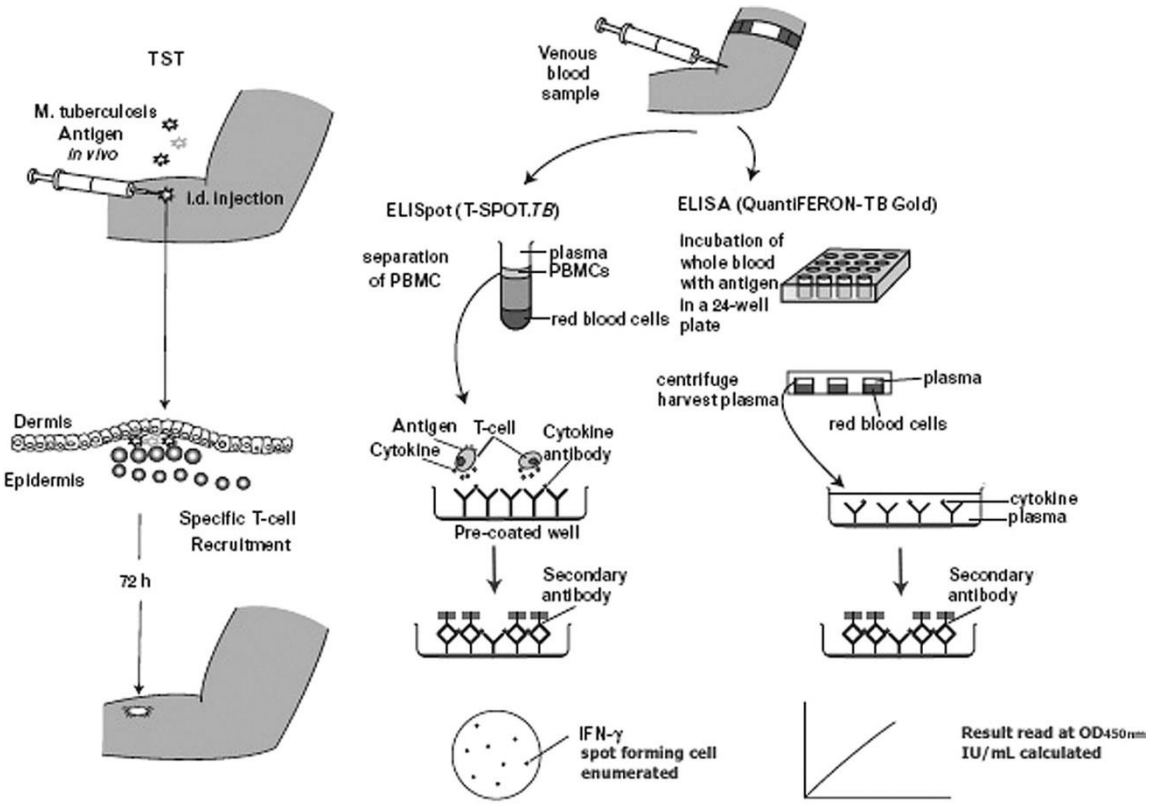

Figure 2: Schematic diagram of TST (left), ELISpot (center), and ELISA (right) for diagnosing Tuberculosis infection [11]

TB blood tests (also called interferon-γ release assays or IGRAs) measure how the immune system reacts to the TB bacteria. An IGRA measures how strong a person's immune system reacts to TB bacteria by testing the person's blood in a laboratory. Recent *Mycobacterium* genomics studies in the late 1990's have identified a specific Mtb genomic segment named region of difference-1 (RD-1), that is deleted from all strains of BCG vaccine and non-tuberculosis environmental mycobacteria. Two proteins produced by genes in RD-1, early secretory antigenic target-6 (ESAT-6) and culture filtrate protein-10 (CFP-10), are targets of T-cells in TB patients. The T-cells produce a complex response

to these antigens, including specific cytokines. These assays work by detecting a cytokine called the interferon-γ cytokine. There are two IGRA blood tests that are commercially available for measurement of antigen-specific T-cell responses and have been approved by the U.S. Food and Drug Administration (FDA) and in some European countries: the QuantiFERON® TB Gold test, and the T-SPOT® TB test [2, 11, 12].

The QuantiFERON® TB is based on whole blood enzyme-linked immunosorbent assay (ELISA) (developed in Australia in 1980, adapted for human use in the 1990s). The QuantiFERON® TB is a whole-blood ELISA, which measures the interferon (IFN) -γ concentration in the supernatant of a sample of diluted whole blood after 24 h of incubation with ESAT-6 and CFP-10 (Figure 2, right). This blood test has been recommended to replace TST. T-SPOT® TB test is based on ELISpot developed in UK in 1990. ELISpot is a rapid ex-vivo enzyme-linked immunospot assay which counts individual antigen-specific T cells. In the presence of Mtb Infection, T cells become sensitized to ESAT-6 or CFP-10 in-vivo. In the overnight ELISpot assay, they release a cytokine, interferon (IFN)-γ as they re-encounter these antigens ex-vivo (Figure 2, center). Compared to the other techniques, these blood tests are faster and simpler than microscopy techniques, more sensitive in detection of false negative LTBI cases and fewer false positive cases in BCG vaccinated people than TST [2, 11, 12].

Sputum smear microscopy remains the primary tool for the diagnosis of pulmonary tuberculosis in low-income and middle-income countries. It requires simple and inexpensive laboratory facilities, and when performed correctly, has an important role in rapidly identifying infectious cases specifically in areas where there is a high prevalence

of TB. However, sputum microscopy has several limitations for the diagnosis of TB in children and in HIV-positive individuals (smear-negative TB). Smear microscopy involves collecting two consecutive sputum specimens, fixing them on a glass slide, and then staining them with a dye that binds specifically to mycobacteria (making them easier to identify under a microscope). Smear microscopy for TB is sometimes called AFB testing, because mycobacteria are 'acid-fast bacilli' (AFB). This means that certain dyes adhere to the waxy coat of mycobacteria and remain visible even after rinsing with water and being briefly treated with a solution of acid-alcohol that strips the dye from the rest of the smear. Sputum microscopy can be used to diagnose people with infectious TB, monitor the progress of treatment, and confirm that the cure has been achieved [13, 14].

Culture is used to diagnose active Mtb infections, infections due to nontuberculous mycobacteria, or to determine whether TB-like symptoms are due to another cause. Sputum cultures can also be used to monitor the effectiveness of treatment and can help determine when a person is no longer infectious. Though this test is more sensitive than sputum smear microscopy, it takes longer for results to become available due to the slow growth rate of Mtb, which may take several weeks to months. Currently, sputum culture is the most sensitive technique for TB diagnosis [15].

Chest X-ray is usually done when the TB skin test result is positive or in the presence of symptoms of active TB such as a persistent cough, high fever, fatigue, or night sweats. An uncertain reaction to the TB skin test would require an X-ray because of a weakened immune system or a previous BCG vaccination. Chest X-rays may reveal advanced pulmonary TB, but can miss other less obvious forms [11, 12].

Different approaches can be used for TB diagnosis, based on the available facilities and the infection stage (LTBI or pulmonary TB). Table 1 summarizes different approaches for TB diagnosis based on the different regions of the world.

After completion of treatment for pulmonary TB, patients remain at risk for complications, including relapse (rates of 0-6% within 6 to 30 months), aspergilloma, bronchiectasis, broncholithiasis, fibrothorax, and possibly carcinoma. A copy of the chest radiograph at the time of completion of therapy should be provided to the patient to facilitate the diagnosis of late complications. Relapse after treatment indicates that viable Mtb complex may remain after treatment in some patients. Rate of relapse is higher in certain populations such as AIDS patients, non-compliant patients, and patients infected with resistant strains of Mtb. Methods to identify patients at risk of relapse and methods to monitor response to treatment would be desirable. Since radiographic resolution lags behind clinical improvement, sputum microscopy and sputum culture are currently the methods used to monitor the efficacy of treatment and outcome. However, since sputum microscopy is insensitive and sputum culture is time-consuming, supplementary rapid and sensitive monitoring methods would be advantageous [15].

Table 1: TB diagnosis approaches in different regions

Region		Approaches
High burden of TB	Sub-Saharan Africa	• Sputum smear acid-fast microscopy (pulmonary TB); takes multiple days to get the results • Sputum culture (pulmonary TB); takes weeks for results • Chest X-ray if sputum smear result was negative (pulmonary TB)
	India	• Sputum smear acid-fast microscopy (pulmonary TB); 1 day to weeks to get results • Chest X-ray (pulmonary TB)
	China	• Chest X-ray (pulmonary TB) • Sputum smear acid-fast microscopy (pulmonary TB); 1 day to weeks to get results • Sputum culture (pulmonary TB); takes weeks for results
Moderate burden of TB	Eastern Europe & Russia	• Chest X-ray (pulmonary TB) • Sputum smear acid-fast microscopy (pulmonary TB); usually same day results • Sputum culture (pulmonary TB); takes weeks for results
	Central & South America	• Skin test (LTBI); takes 1-2 days for results • Blood test (LTBI); takes 1-2 days for results • Chest X-ray (pulmonary TB) • Sputum smear acid-fast microscopy (pulmonary TB); 1 day to weeks to get results • Sputum culture (pulmonary TB); takes weeks for results
Low burden of TB	Western Europe, US & Canada	• Skin test (LTBI); takes 1-2 days for results • Blood test (LTBI); takes 1-2 days for results • Chest X-ray (pulmonary TB) • Sputum smear acid-fast microscopy (pulmonary TB); same day results • Sputum culture (pulmonary TB); takes weeks for results • Gastric aspirate smear acid-fast (pulmonary TB); pediatric diagnosis; same day results • Gastric aspirate culture (pulmonary TB); pediatric diagnosis; same day results; takes weeks for results

2.3 Fluorescence markers for TB detection

The use of green fluorescent protein (GFP), from the jelly fish *Aequorea victoria*, as a marker of gene expression in the nematode *Caenorhabditis elegans* was first introduced in 1994 [16]. During the next 15 years, a variety of fluorescent proteins (FPs) spanning the visible spectrum were introduced and developed. The emission peak of most FPs that are derived from GFP are in the blue, green, or yellow spectral range. Red FPs such as DsRed are mostly derived from other sea organism like *Discosoma sp*.

Appropriate excitation and emission wavelengths, photostability (the time for a FP to lose 50% of its initial emission), maturation speed (the time to form a full chromophore), and brightness (quantum yield × extinction coefficient) are some of the criteria for a fluorescent marker to be suitable for use in biophotonic imaging (BPI). Fluorescent markers in the red or the far red region of the spectrum are more suitable for BPI, because of the reduced absorption and deeper light penetration of red and near infrared (NIR) wavelengths in tissue [17, 18]. Table 2 summarizes some of the FPs that have been used to study bacterial infection.

Table 2: Properties of the most suitable fluorescent proteins for BPI [18, 19]

Class	Protein	Excitation (nm)	Emission (nm)	Origin	Brightness (% DsRed)	Photostability	Maturation time (min)
Far-red	mPlum	590	649	DsRed	7	53	100
Red	mCherry	587	610	DsRed	27	96	15
	tdTomato	554	581	DsRed	160	98	60
	DsRed	558	583	*Discosoma* sp.	100		~600
Yellow-Green	EYFP	514	527		86	60	
Green	EGFP	488	507	*Aequo ea victoria*	57	174	

2.4 Biophotonic imaging techniques for bacterial detection

Since the current techniques for monitoring TB over time in preclinical animal studies are costly and time consuming for processing (animal sacrifice, organ harvest, tissue homogenization, and colony forming units (CFU) counts that may take up to 6-weeks) [18], the development of sensitive experimental techniques that could provide rapid feedback regarding the therapeutic and vaccine efficacy in animal models could greatly benefit the development of TB vaccines and treatment strategies. Optical sensing and imaging offers a promising noninvasive solution to monitor bacterial dynamics in the host over time with high sensitivity. Optical imaging techniques have been used in a wide variety of applications such as visualizing tissue anatomy on the microscopic scale using reflectance spectroscopy [19], pre-cancer detection using confocal microscopy [20], and noninvasive localization of a photonic signal using fluorescence whole animal imaging [21, 22] (Table 3).

Table 3: Optical imaging methods. A, absorption; Fl, fluorescence; S, scattering; E, emission [11]

Resolution	Technique	Contrast	Depth
Microscopic	Epi-microscopy	A, Fl	20 μm
	Confocal microscopy	Fl	500 μm
	Multiphoton microscopy	Fl	800 μm
Mesoscopic	Optical projection tomography	A, Fl	15 mm
	Optical coherence tomography	S	2 mm
	Laser speckle imaging	S	1 mm
Macroscopic	Hyperspectral imaging	A, S, Fl	< 5 mm
	Endoscopy	A, S, Fl	< 5 mm
	Fluorescence reflectance imaging (FRI)	A, Fl	< 7 mm
	Diffuse optical tomography (DOT)	A, Fl	< 20 cm
	Fluorescence resonance imaging (FRI)	A, Fl	< 7 mm
	Fluorescence molecular tomography (FMT)	Fl	< 20 cm

BPI of luciferase-catalyzed reactions (bioluminescent) or excited fluorescent molecules is a highly sensitive optical imaging technique, which allows real-time noninvasive assessment of microorganisms and their locations within intact living animals. BPI is achieved using sensitive photon detectors to directly measure the visible (VIS) light produced by these microorganisms [18]. As light travels through different organs (such as skin, muscles, and bones), the light distribution and light propagation can be observed and quantified within living animals. Recently, commercial optical imaging systems have been widely used to study the molecular and cellular mechanisms that underlie disease development and progression (Table 4).

“Replacement” methods that avoid or replace the use of animals, “reduction” methods that minimize animal use, and “refinement” methods that minimize the animal’s pain, suffering, and distress are the “three R’s” that many countries promote as ethical

responsibilities when using animals in research. BPI techniques can result in refinement and reduction. Using conventional methods for modeling infectious diseases, large numbers of infected animals per group are sacrificed at specific time points for bacterial enumeration from excised tissue.

However, using BPI techniques, which allow for real-time monitoring of infected animals simply by detecting and imaging the optical signal within one group of animals, the same experiment could be completed with just 6 to 8 animals. In addition, real-time monitoring of the same group of animals over time, allows for following the disease progression more precisely, by having each animal as its own control [18]. Furthermore, detected bioluminescence and fluorescence signal in BPI techniques can be used for quantification of bacterial numbers, which can result in significant refinements in in-vivo animal experiments, since the photonic signal can be used to estimate whether the animal will survive or die [22-24]. BPI techniques can also reduce the level of pain and/or stress for animals by reducing the need for invasive sampling procedures that may be needed for bacterial quantification in specific organs or fluids such as blood [25]. Finally, effectiveness of the inoculation method can also be evaluated by real-time data provided by BPI techniques, so any administration errors can be detected immediately, minimizing unnecessary pain, suffering, and discomfort for the animals [18].

Table 4: Commercially available BPI instrumentation [19]

Manufacturer	Instruments	Features	Specifications
Berthold Technologies	NightOwl	Bioluminescence; Fluorescence	Various filters; tungsten halogen excitation source.
Biospace Lab	PhotoImager	Bioluminescence; Fluorescence; Image freely moving animals	Wide range excitation/emission filters; halogen excitation source.
Perkin Elmer	IVIS (various models)	Bioluminescence; fluorescence; Digital X-ray; Image freely moving animals	Wide range excitation/emission filters; software for 3D reconstruction using spectral scanning.
Cambridge Research & Instrumentation (CRi)	Maestro	Fluorescence; Spectral scanning	Tunable filter allows spectral scanning; xenon excitation source.
Carestream Health	Kodak *In - vivo* Imaging Systems	Bioluminescence; fluorescence; Digital X-ray	Various excitation/emission filters; xenon excitation source.
Li-Cor Biosciences	Pearl; Odyssey Imager + Mousepod	NIR fluorescence	2-channel laser excitation
VisEn	FMT 2500 Imaging system	NIR fluorescence; Reflectance imaging and Quantitative Tomography Multimodality adaptors for CT/MR/PET	2-channel laser excitation
UVP	iBox Scientia Small Animal Imaging	Bioluminescence; Fluorescence	Various excitation/emission filters

2.4.1 Properties of light propagation through tissue

Different factors can affect the sensitivity of the BPI techniques, such as: sensitivity of the detection system, level of fluorophore/luciferase excitation, excitation/emission wavelength, tissue type and tissue depth, whether the animal has fur or is pigmented, and tissue auto-fluorescence/luminescence background. However, the main challenges in optical imaging are related to light propagation through tissue (scattering and absorption), and tissue auto-fluorescence background signal within living animals [18].

When VIS or NIR photons interact with tissue, they highly scatter within the tissue and follow a diffusive path. In addition, their intensity (I) reduces after passing through tissue depth (d) based on the Beer-Lambert law $I(d) = I_0 e^{-\mu d}$, where μ is the coefficient of absorption and I_0 is the incident intensity [26] . Endogenous chromophores, especially hemoglobin within the VIS range (400-760 nm), absorbs light within tissues in the blue and green part of the VIS spectrum, however its absorption reduces in longer wavelengths (> 600 nm), which allows red light transmission through several centimeters in tissue [27]. In addition to hemoglobin, melanin also contributes in light absorption in pigmented animals, so using albino animals for any optical imaging will minimize this problem. Due to the different interactions of light within the tissue and its significant impact on how much excitation light can travel from the surface to the target tissue, there is a high demand to develop highly sensitive optical imaging techniques that can reduce tissue absorption and auto-fluorescence.

Bioluminescence imaging techniques that rely on light-tight enclosures and transgenic cells expressing the enzyme luciferase are more sensitive than fluorescence imaging techniques because of the higher signal-to-noise ratio. The level of tissue auto-fluorescence background in-vivo is higher than luminescence background; auto-fluorescence is due to endogenous fluorophores such as keratin, porphyrins, NADH, collagen and elastin. Auto-fluorescence is almost uniform in the green and red spectral regions over the entire animal, however it is more concentrated in the intestinal area in far-red and NIR spectral regions, due to the presence of chlorophyll in the animal's diet [28]. Alternative available diets such as alfalfa-free diet and a purified diet can significantly reduce the level of tissue auto-fluorescence in the red and NIR region [29]. Also, using advanced spectral unmixing algorithms can improve the signal-to-noise ratio by separating auto-fluorescence background from the specific signal [30].

2.4.2 Fluorescence imaging

Optical fluorescence imaging is an increasingly widespread technique in biology due to advances in fluorescent proteins, dyes, and probes that facilitate noninvasive imaging of gene expression, protein functions and interactions, and a variety of cellular processes [31, 32]. Different fluorescence imaging techniques offer imaging from the range of macroscopic imaging (small-animal whole-body imaging) to microscopic resolution imaging and video-rate scans [33-35], as well as methods that can operate at resolution beyond the diffraction limit and image single molecules.

2.4.2.1 Overview of whole animal imaging

Whole-body fluorescence optical imaging of animal models is a new and promising technique to study the molecular and cellular mechanisms that underlie disease development and progression, as well as gene expression by employing co-expression of fluorescent markers. This optical imaging technique has been widely used in noninvasive cancer studies, growth monitoring of tumors, and the effects of chemotherapy on tumor size using recombinant fluorescent cancer cells [21, 36-39], and recently in the study of bacterial infection dynamics [40].

In whole-body imaging, the subject is illuminated with a broad-band light passing through an excitation filter, which is specified for the excitation wavelength of the fluorophore of interest. Whole-body optical imaging can be performed in epi-illumination and trans-illumination. In epi-illumination mode, the light source is located on the same side of the body as the detector; in contrast, in trans-illumination mode, the light source is located on the opposite side of the body from the detector [18]. Figure 3 shows the schematic of the trans-illumination IVIS spectrum whole-body imaging system. Trans-illumination mode generally is more efficient in imaging signals located deeper inside the body. The resulting emission signal collected from the whole body is then captured in a completely dark chamber. Depending on the strength and location of the fluorescence signal, image acquisition can take from seconds to minutes. Specific bandwidth emission filters are selected to capture the desired emission spectrum. High sensitivity detectors have enabled detection of low numbers of cells in-vivo excited by epi- or trans-illumination. CCD cameras encode the intensity of the incident photons spatially, which

are shown as pseudo color images overlapped on the photographic images for spatial registration. To evaluate the results, data are quantified over the region of interest and reported as photon flux or photon efficiency [18].

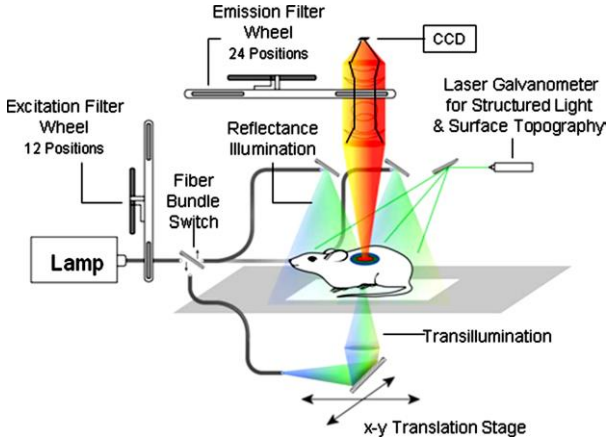

Figure 3: Schematic of the IVIS spectrum imaging system [31]

Whole-body imaging has some intrinsic limitations related to the interaction of light with tissue components. Light scattering and absorption by tissue components cause signal attenuation and loss of resolution, and will diminish the ability to detect and resolve small populations of cells or pathogens deep inside the animal body, such as in the lung. Additionally, contribution of autofluorescence in the visible range, particularly from skin in epi-illumination, increases background and complicates signal detection even with spectral unmixing techniques. Figure 4 shows how light scattering and absorption can affect detected fluoresce signal in living tissue using simulated mouse models, imaged in epi-illumination mode. A tumor was located in the abdomen of each simulated animal,

one close to the skin surface and the other near the axial center of animal. As figure 4 shows, the intensity of the fluorescence signal coming from the tumor is dependent on its depth within the body [41].

Whole-body imaging, both in bioluminescence and fluorescence modes, has been used for the detection and imaging of different types of bacteria. Detection thresholds for whole-animal imaging of various types of bacterial infections is summarized in Table 5.

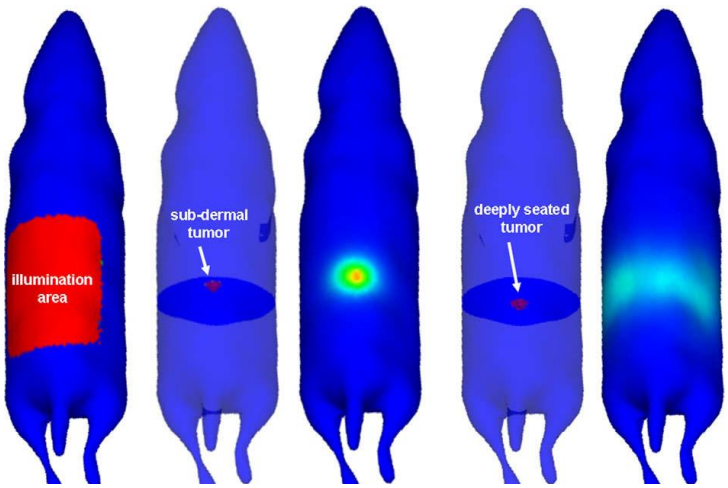

Figure 4: Simulated mouse models to show how photon scattering can affect the fluorescence intensity in living tissue. A tumor was located in the abdomen in each model: (b) near the surface, (d) close to the axial center. (a) Shows the illuminated area by epi-illumination imaging. (c) and (e) show the detected fluorescence signal for the tumors in (b) and (c), respectively [42]

Table 5: Whole-animal imaging detection limit for bacterial detection

Bacteria	Fluorescent probe	Infection rout	Location of bacteria	Imaging Modality	Detection limit (CFU)	Reference
Citrobacter rodentium	-	Oral	In-vivo (gut)	Bioluminescent	10^3	[42]
S. aureus	-	Subcutaneous Thigh injection	In-vivo (subcutaneous, muscle tissue)	Bioluminescent	10^5 (subcutaneous), 10^6 (muscle)	[43]
M. *bovis* BCG	EGFP	subcutaneous	In-vitro	Fluorescence Trans-illumination	10^3	[40]
M. *bovis* BCG	tdTomato	subcutaneous	In-vitro	Fluorescence Trans-illumination	10^2	[40]
M. *bovis* BCG	EGFP	subcutaneous	In-vivo (subcutaneous)	Fluorescence Trans-illumination	10^7	[40]
M. *bovis* BCG	tdTomato	subcutaneous	In-vivo (subcutaneous)	Fluorescence Trans-illumination	10^5	[40]
M. *bovis* BCG	CNIR5	Intratracheal Aerosol	In-vitro	Fluorescence Trans-illumination	10^2	[44]
M. *bovis* BCG	CNIR5	Intratracheal Aerosol	In-vivo *(Lung)*	Fluorescence Trans-illumination	10^4	[44]

2.4.2.2 Overview of fiber-optic fluorescence microscopy

Optical fiber-based sensing and imaging techniques have been used in numerous areas of in-vivo studies and clinical practice. Optical fiber bundles have been exploited in high resolution confocal microendoscopes with high numerical aperture miniature objective lenses [45-47]. Simplified contact probe microendoscopes with wide-field illumination have more recently been developed [31, 48-50] and evaluated as tools for cancer detection [38, 51, 52].

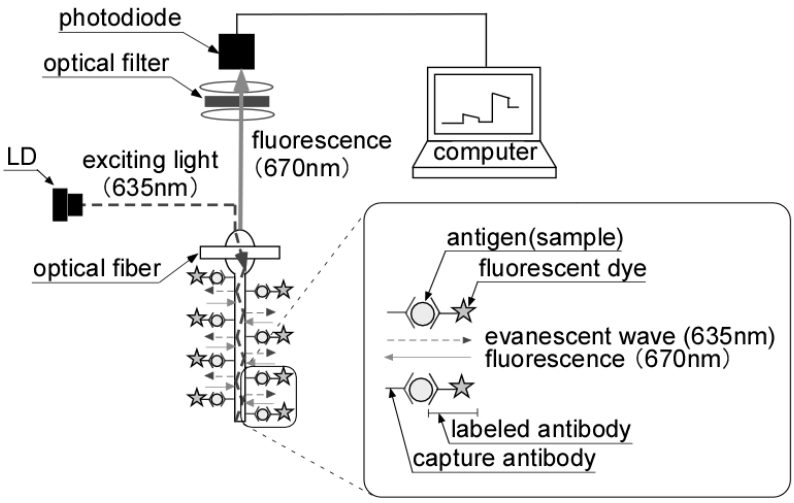

Figure 5: Fluorescent immunoassay using optical fiber [57]

Fiber optic techniques have been used for bacterial detection and sensing in biological samples. Fiber optic biosensors (FOB) have been employed to convert the laboratory-based detection systems to smaller and more portable detection systems to allow the detection of whole bacterial cells [53, 54]. FOB usually composed of a light source which

generates the excitation light and an optical fiber containing immobilized bioreceptors, which transfer the excitation light to a sensitive detector [55]. A fiber-optic immune-sensor has been developed for detection of *Escherichia coli* and *Listeria* monocytogenes in samples using Cynine-5 (Cy5) labeled polyclonal antibody (figure 5). Excitation light from the optical fiber excites Cy5 molecules, and the emitted fluorescence light is collected using a sensitive photodiode [56].

It has been shown that fiber-based intravital microendoscopy has the potential to image and detect low numbers of bacteria *in vitro* and *in situ*. A fiber-optic microendoscope with 4 μm resolution and 750 μm field of view has been developed to image mice subcutaneously and intra-tracheally infected with bacteria expressing tdTomato. The results show that the microendoscope's limit of detection was 10^4 CFU in the case of skin samples and 10^7 CFU for lung samples [31]. By physically transmitting the excitation light source to the source of fluorescence in the tissue, detection levels can be greatly reduced, approaching the *in vitro* detection levels of whole-body imaging systems. Furthermore, intravital imaging of low numbers of bacteria with subcellular resolution may enable cellular localization of bacteria within the tissue and help to get a better understanding of dynamic processes in a minimally invasive manner.

CHAPTER III

SMALL ANIMAL INFECTION AND IMAGING

3.1 Introduction

Small animal models play an important role in the study of cellular and molecular function and disease. Well-defined animal models allow the assessment of their biology, and provide useful information about different disease processes in its natural context in-vivo, rather than in reductionist systems such as cells in culture dishes or on slides [18, 57, 58].

Among the wide variety of animal models to evaluate and test antibiotic drugs and vaccines, mice are the most widely used since they are relatively low cost, have a low animal-to-animal variability because of the availability of inbred strains, have a lifespan of 3 years, and have extensive physiological and molecular similarities to humans. Mice also need a smaller area for housing compared to other animals, such as guinea pigs and rabbits, and a large number of them can be housed in standard cages. Mice infected with strains of *Mycobacterium tuberculosis* are used as a model of the host protective immune response, since they are relatively resistant to mycobacterial infections [58-60].

3.2 Small animal infection with mycobacteria

Infection with mycobacteria can be accomplished by a variety of routes, including intravenous inoculation of mice via the lateral tail vein or aerogenic routes. However, *Mycobacterium* infection via aerogenic route is the most physiologically normal way to

model human disease, since the natural route for tuberculosis infection in humans is the lung tissue. Mouse lungs can be infected intranasally or intratracheally. An aerosol of small droplet nuclei containing bacilli can be generated so that the inhalation of these droplets by the animal deposits them deeply into the alveoli of the lungs [59].

Following infection with mycobacteria, animals should be observed daily, and clinical symptoms recorded. Information such as daily body temperature and weight are useful to evaluate disease progression. In general, the progress of disease has five stages, based on the involvement of granulomatous, the cell types, the degree of lymphocyte organization, and the presence of destructive sequelae such as airway epithelium erosion and debris [61].

3.1.1 Preparation of mycobacterial cultures for inoculation

Mycobacterial frozen stocks, either *M. bovis* BCG strains or *M. tuberculosis* strains, are routinely grown in culture both at 37˚C until an OD_{600}=0.5 to 1 is obtained. Cultures can be stored in half medium/half sterile glycerol at −80˚C until use. In order to use the mycobacterial culture, the OD_{600} is measured and bacterial density determined based on this value. In general $OD_{600} \approx 1.0$ represents 1.0×10^7 bacteria/ml for *M. tuberculosis* and *M. bovis* BCG. The target bacterial density can be calculated based on the initial density and the inoculation prepared by dilution or concentration of the initial culture [22].

3.1.2 Routes of administration

Administration of test substances, such as bacteria or fluorescent marker, to mice is one the most important experimental factors considered for evaluation of experimental results. The route of administration is dependent on the purpose of the experiment and the properties of the substrate. Mice should be protected from pain, distress, suffering, or at least these should be minimized. Among several ways to administer the bacteria or substrate to mice, the most common routes are subcutaneous (s.c.), intraperitoneal (i.p.) and intravenous (i.v.) injection, and intratracheal administration. The rate of absorption depends on the administration route. The bacteria/substrate usually absorbs immediately following i.v. injection, which is usually one-half or one-quarter as rapid as the other routes [62].

3.1.2.1 Subcutaneous administration (s.c.)

Subcutaneous administration is usually easy and painless, such that a conscious mouse can be used. However, the absorption rate is lower than i.p. or i.v. injections. S.c. administrations is usually done over the interscapular or inguinal area in mice [62].

3.1.2.2 Intraperitoneal administration (i.p.)

Intraperitoneal injection is the most common administration route, since it is technically simple to do. The absorption rate is longer than the i.v. route. The sensitivity of the tissue to substance and the lower tolerance to non-physiological pH of some solutions are potential limitations of this technique. Isotonic and large volume solutions can be administrated by this route [62].

3.1.2.3 Intravenous administration (i.v.)

Intravenous injection has some advantages over the other routes. Solutions with different pH level, high concentrations, or irritating elements can be administered via i.v. injection by keeping the injection rate slow and avoiding getting the solution outside of vein. Administration is usually made into the lateral tail vein, not into the dorsal tail vein. Other routes for i.v. injection such as ophthalmic plexus route, external jugular vein route, dorsal metatarsal vein route, and the sublingual vein route have been also reported [62].

3.1.2.4 Intratracheal administration

In order to infect the mouse intratracheally, each animal is injected with a mixture of ketamine (100 mg/kg) and xylazine (10 mg/kg) for anesthesia. After the mouse is deeply anesthetized, using an otoscope and a guide wire, the catheter will be placed into the larynx. After placing the catheter, 50 µl of the bacterial solution will be pipetted on to the hub of the catheter followed by pipetting a small volume of air, to make sure all the solution is inhaled by the animal [22].

3.1.3 Bacterial enumeration

After in-vivo experiments, determination of bacterial numbers can be accomplished by a number of direct or indirect methods, including standard plate counts, turbidimetric measurements, visual comparison of turbidity with a known standard, direct microscopic counts, cell mass determination, and measurement of cellular activity. In this project, we have performed bacterial enumeration after each in-vivo experiments using the standard plate count method, as described below.

A viable cell count is usually done by diluting the original sample, plating aliquots of the dilutions onto an appropriate culture medium, and then incubating the plates under proper conditions until colonies are formed. After incubation, the colonies are counted and, from knowledge of the dilution used, the original number of viable cells calculated. For accurate determination of the total number of viable cells, it is critical that each colony comes from only one cell, so chains and clumps of cells must be broken apart. However, since one is never sure that all such groups have been broken apart, the total number of viable cells is usually reported as colony-forming units (CFU) rather than cell numbers. This method of enumeration is relatively easy to perform and is much more sensitive than turbidimetric measurement. A major disadvantage, however, is the time required for dilutions, platings and incubations, as well as the time needed for media preparation.

3.2 Small animal imaging

Imaging of small laboratory animals (such as mice and rats) allows a noninvasive technique to evaluate in-vivo biological structures and functions, providing quantitative information on normal and/or diseased tissues. In addition, noninvasive small animal imaging facilitates longitudinal study of animal models of human diseases such as cancer, cardiovascular, and bacterial infections over the entire disease progression period, and monitoring of efficacy of different treatments and vaccines [63].

In this study, all animals were anesthetized with ketamine (100 mg/kg) and xylazine (10 mg/kg) before imaging. Animals were kept warm using a temperature-controlled plate during and after imaging until they fully recovered from the anesthesia.

All imaging procedures were performed with great care to avoid tissue damage or animal suffering.

CHAPTER IV

INTEGRATION OF WHOLE-ANIMAL OPTICAL IMAGING WITH FIBER OPTIC EXCITATION

4.1 Introduction

In this study, we developed a fiber based excitation source/microendoscope that is coupled into a whole-animal imaging system in order to allow the excitation light to be delivered inside an animal model. This greatly enhances the intensity that can be achieved inside the animal, as the optical path length through tissue between the source and expected location of the fluorophore is minimized. In addition, such a system facilitates multi-scale imaging, where microscopic imaging can be obtained simultaneously with macroscopic whole-animal images in the case of using an imaging fiber bundle in the designed system.

4.2 Intravital excitation sources for whole-animal imaging

Three different optical fibers have been used in conjunction with whole-animal optical imaging to deliver the excitation light internally to improve the detection threshold of respiratory bacterial infection inside live animals, and their performances have been evaluated and compared; 1) a multimode fiber with 400 μm diameter core size (Thorlabs FT400UMT); 2) a diffuser fiber with 420 μm outer diameter; and 3) an optical imaging fiber bundle with 660 μm outer diameter (Fujikura FIGH-10-500N). Imaging studies were

performed using 1) fiber-based intravital excitation and whole-animal imaging with the IVIS illumination blocked, and 2) IVIS epi-illumination and detection for comparison.

4.2.1 Fiber optic microendoscope

Figure 6 illustrates the schematic of the fluorescence microendoscope that was constructed for bacterial detection and integrated into the whole-animal imaging system. The designed system can be used as an excitation source and/or as a microendoscope for multi-scale imaging. The basic design is similar to the system previously reported for use in bacterial imaging in situ [31]. A light source [light emitting diode (LED) or laser diode (LD)] is used for fluorescence excitation. Light from the source is filtered with an excitation filter, collimated with a condenser lens, and reflected off a dichroic mirror into the back aperture of an infinity-corrected objective lens focused on an optical fiber. Excitation light is guided by the optical fiber to its distal tip, which can be inserted into the airway of an animal model through an intratracheal catheter. For multiscale imaging purposes, the fluorescence emission light is then collected by the same or different fiber, filtered by a long-pass emission filter, and then focused onto a scientific grade 1.45 megapixel CCD camera (QImaging Exi Blue) with 6.45 μm x 6.45 μm pixel size. All the

optical components of the microendoscope could be easily modified based on the desired fluorescent probe and its optical properties.

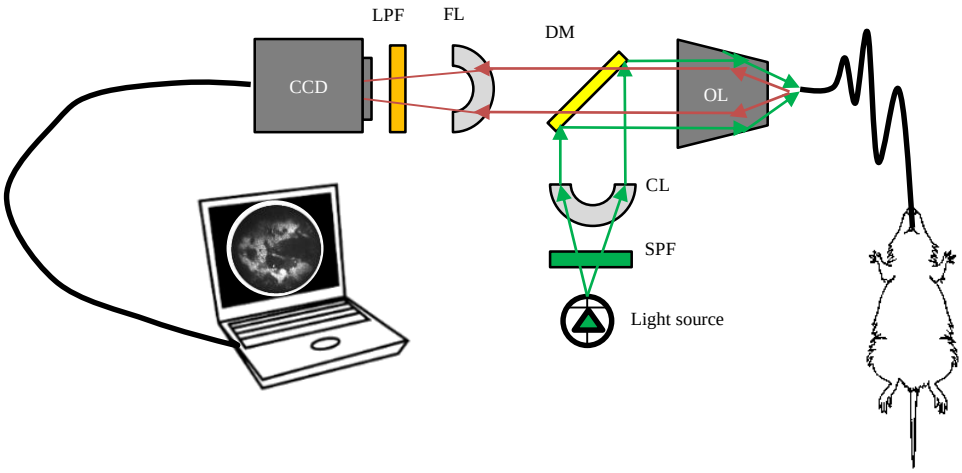

Figure 6: Illustration of the fiber-based microendoscope system. SPF: short-pass excitation filter; CL: collimating lens; DM: dichroic beamsplitter; OL: Microscope objective; FL: Focusing lens; LPF: long-pass emission filter.

4.2.2 Fiber optic diffuser

To enhance the excitation efficiency of fluorescent probes in the lung and reduce fluorescence background for whole animal fluorescence image detection, a fiber-coupled diffusing tip was fabricated and developed to illuminate the lumen of the airway, and its efficiency evaluated and compared to a multimode fiber and fiber bundle. The fiber diffuser was fabricated by casting a polymer rod (post-polymerized, UV-crosslinked, thermoset polyurethane) over the tip of the excitation fiber and media blasting the polymer to create defects, generating a light diffusing surface [64]. The length and width of the

diffuser were optimized for transport through an endotracheal catheter in the mouse lung. Initial optical diffuser target metrics were ~5 mm in length to protrude past the tip of the catheter, and 420 µm in diameter to pass through the 600 µm inner diameter catheter. An image of a joint between an optical fiber and a cast SMP rod is shown in figure 7.

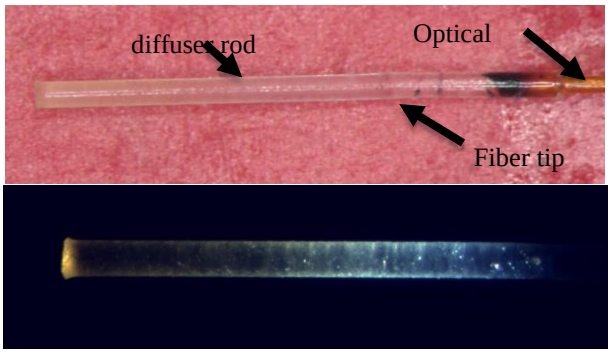

Figure 7: Microscope image of an SMP diffuser showing attachment to the optical fiber and light distribution over the length of the diffuser. Magnification of the scope: 0.65

An integrating sphere was used to measure the diffusion efficiency. The total radiant power emitted from the diffuser, including the light emitted from the diffusing surface and from the distal tip was measured by inserting the entire diffuser through an aperture slightly larger than the diffuser diameter into the integrating sphere. The diffuser was then withdrawn in 2-mm increments, and the power emitted from the distal portion inside the sphere was measured. The diffusion efficiencies over axial distances of 2, 4, 6, and 8 mm of the diffuser length were 8.5, 20, 36.7, and 58%, respectively. The percentage

of incident light exiting the distal end of the diffuser was 42%, equal to the difference between the diffusion efficiency over 8 mm and 100%. A perfectly uniform diffuser with a diffusion efficiency of 96% over 8 mm would have values of 24, 48, 72, and 96% diffusion efficiency measured at 2, 4, 6, and 8 mm axial length, with 4% exiting the tip [64].

To measure the axial light emission profile along the length of the diffuser, an 800 nm laser was used to illuminate the fiber with the attached 5 mm diffuser tip. The diffuser was manually rotated and reimaged to evaluate the circumferential uniformity. Figure 8 shows the axial light emission profile along the 5 mm length of diffuser.

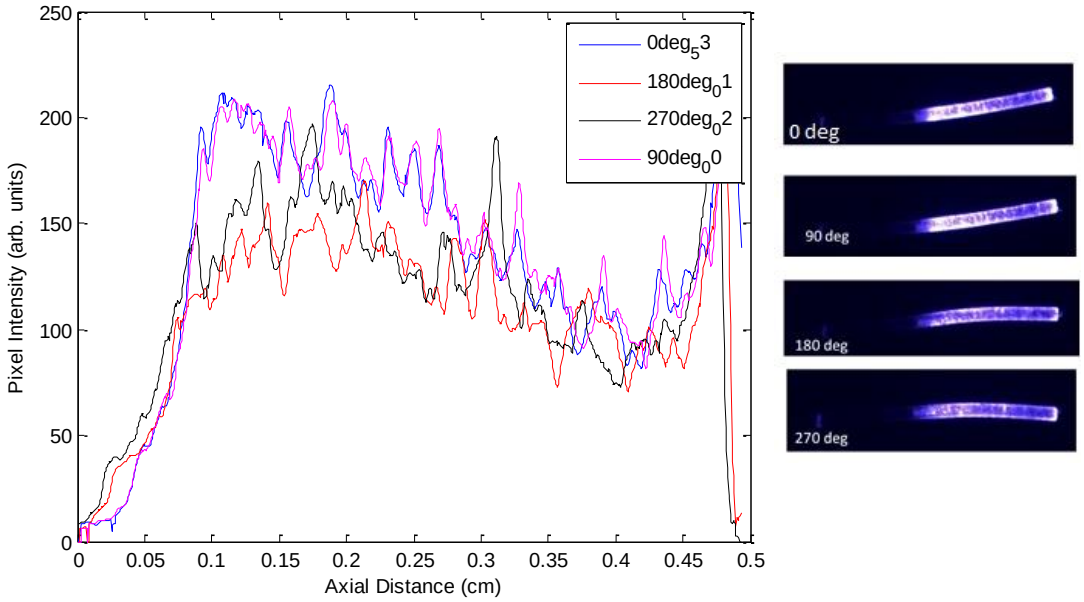

Figure 8: Axial light emission profile and circumferential uniformity of the diffuser tip attached to an optical fiber.

4.2.3 Integration of intravital excitation with whole-animal imager

Multi-scale imaging of bacterial infections was achieved by integrating the fiber excitation source or microendoscope into a whole animal imager (Perkin Elmer IVIS Lumina II). The fiber was inserted into the whole animal enclosure through an access port located on the side of the system, shown in figure 9. To prevent any external light from entering the system, a 0.5 mm hole was drilled into a rubber stopper (VWR 59580-069) which was then inserted into the access port opening. The fiber was then inserted through the hole in the rubber stopper, as shown in figure 9(B).

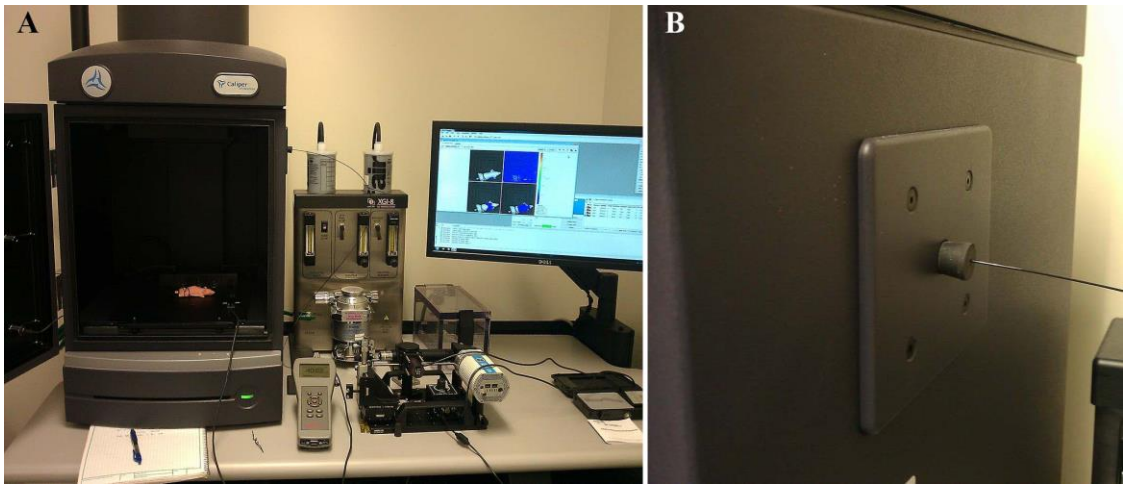

Figure 9: Integration of the fiber excitation source with the IVIS whole-animal imaging system. (A) Both optical systems on the same bench top. (B) The fiber is coupled via a test tube stopper placed into the access port of the IVIS system.

4.3 Spectral unmixing

To reduce the effects of tissue autofluorescence and quantify the fluorescence signal for each individual fluorophore in both in-vivo and ex-vivo experiments, all whole-body images were post-processed using spectral unmixing with Living Image Software (Caliper Life Sciences).

Spectral unmixing is a powerful technique in fluorescence imaging to reduce the effect of natural tissue auto-fluorescence and separate multiple fluorescence spectra from multiple fluorescence probes present in tissue [30]. The spectral unmixing separates image data according to spectra from multiple biophotonic internal light sources in an effort to isolate one or more spectra of interest. Spectral unmixing obtains multiple images, each captured with a combination of different and known excitation and emission wavelength bands. The spectral unmixing then uses an iterative solution process to separate spectra for the multiple light sources, and provides a spectrum and/or a spatial distribution map for at least one of the internal light sources [65]. The basic algorithm for spectral unmixing, as well as the different ways to apply that on whole-body images using the Living Image software, are explained in the following sections.

4.3.1 Fundamental algorithm of spectral unmixing

Linear unmixing is the most common way to process and analyze the images that contain a mixed contribution of localized labels. The basic assumption of linear unmixing is that the spectral properties of each pixel $D(\lambda)$ are a linear combination of individual fluorophores' pure spectra $S(\lambda)$ multiplied by the concentration C plus residue $E(\lambda)$. Therefore the linear unmixing equation would be:

$$D(\lambda) = \Sigma CS(\lambda) + E(\lambda) \quad (4\text{-}1)$$

Equation (3-1) can also be expressed as a matrix form:

$$\mathbf{D} = \mathbf{CS} + \mathbf{R} \quad (4\text{-}2)$$

where **D** is a $m \times n$ spectral data matrix (m corresponds to the number of pixels and n corresponds to the different wavelengths or spectral bands); **C** is a $m \times k$ concentration profile matrix, where each row represents the combination of the mixed fluorophores at that pixel; **S** is a $k \times n$ spectra matrix, in which each row represents the pure spectrum of the corresponding fluorescent probe measured at those wavelengths; and **R** is the $m \times n$ residual matrix which ideally should be close to the experimental error. Based on equation (4-2), **D** is a linear function of both **C** and **S**. In order to calculate the concentration profile based on this linear model, several rules should be followed: 1) all the significant fluorophores present in the image should be addressed in this mode; 2) the number of imaging wavelengths (band-pass filters) should be at least equal to the number of fluorophores needed to detect ($n \geq k$); and 3) the pure spectrum for each fluorophore **S** should be defined beforehand, either measured individually or selected from a pixel that only has one fluorophore. Therefore, concentration profile **C** can be calculated using the below equation [66]:

$$e^2 = \| \mathbf{D} - \mathbf{CS} \|^2 \quad (4\text{-}3)$$

The outputs of this technique are: a) the spectrum of the desired fluorescence probe, and b) the spatial distribution map for that fluorescence probe.

Spectral unmixing is a useful technique even in the case of a single fluorescent probe in an animal. In this case, tissue autofluorescence can reduce the accuracy of the

subsequent image processing, therefore separating its spectrum from the desired fluorescent probe's spectrum is necessary [30, 65].

Living Image software provides four spectral unmixing methods to separate the spectrum of different fluorescent reporters, as well as tissue autofluorescence, and calculate the corresponding contribution of each fluorophore on every pixel of an image.

4.3.2 Spectral unmixing methods

The guided method for spectral unmixing can be used when the location of the fluorescent probe is known, and probe signals are just mixed with tissue autofluorescence, not overlapped with other probe signals. The guided method is a good way to generate a spectral library for probes with known spectra and known locations [67].

The library method uses a user-generated spectrum library to analyze an image set. All the images that are going to be analyzed by this technique must be acquired using the same, or a subset of, the excitation/emission filter pairs of the spectral library. By applying this method for spectral unmixing, the software identifies pixels with spectral characteristics that match the spectra library [67].

Automatic spectral unmixing can be used when the fluorophore's location is unknown. The automatic method uses the pre-defined software's spectral library to analyze the image [67].

Sometimes there is a need to manually analyze the results, especially when the automatic spectral unmixing is unable to distinguish different spectra from each other. When using manual spectral unmixing, tissue autofluorescence signal should be manually

subtracted from the fluorophore's spectrum, to produce the pure spectrum for the desired fluorescent probe [67].

The spectral unmixing results include a signal distribution map of each unmixed result and a composite image of all signals, each displayed in a different color. After spectral unmixing, the signal intensity for each fluorescent probe can be measured over a specific and defined region of interest (ROI).

4.3.3 Comparison of automatic spectral unmixing with manual spectral unmixing

In order to evaluate the different spectral unmixing techniques, a group of five- to seven-week old female BALB/C mice were infected with 10^6 CFU of BCG17 (tdTomato expressing BCG strain) or 10^5 CFU of BCG39 (carry empty plasmid) as a vector control by the intratracheal route.

In order to apply automatic spectral unmixing using Living Image software, a set of images with different emission wavelengths should be loaded. For this specific fluorescent reporter (tdTomato expressing BCG strain), the emission wavelengths were selected from 580 to 640 nm in 20 nm increments. The excitation source from the IVIS was blocked, and the fiber optic illumination source was turned on at 531 nm.

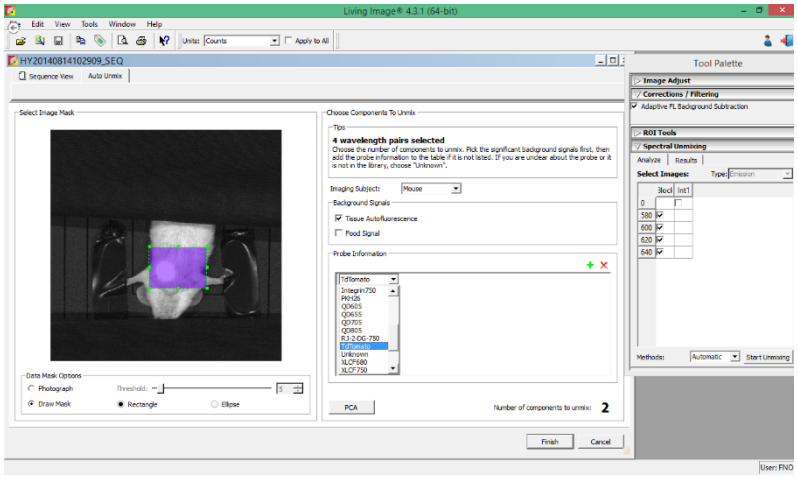

Figure 10: Spectral unmixing window while applying automatic spectral unmixing technique using Living Image software

By selecting the automatic spectral unmixing from the drop-down menu on the "Tool Palette", the Auto Unmix window appears, including a purple data mask showing the region to be included in the analysis. Since the purpose is to detect the bacteria inside the lung, the mask can be drawn on a lung area. The specific fluorophore probe which needs to be separated from tissue autofluorescence can also be selected from the drop-down list (figure 10).

As discussed previously, for automatic spectral unmixing, the software uses its pre-defined spectra for each fluorescent probe, as well as tissue autofluorescence (figure 11). After applying spectral unmixing using this method, the Unmixing window shows the analysis results which include unmixed spectra, unmixed images, and a composite of the unmixed images (figure 12). In figure 12, the unmixed spectra do not match with the expected tdTomato and tissue autofluorescence spectra. This result shows that automatic

spectral unmixing technique is unable to separate tissue autofluorescence spectrum from the fluorescent probe for in-vivo images.

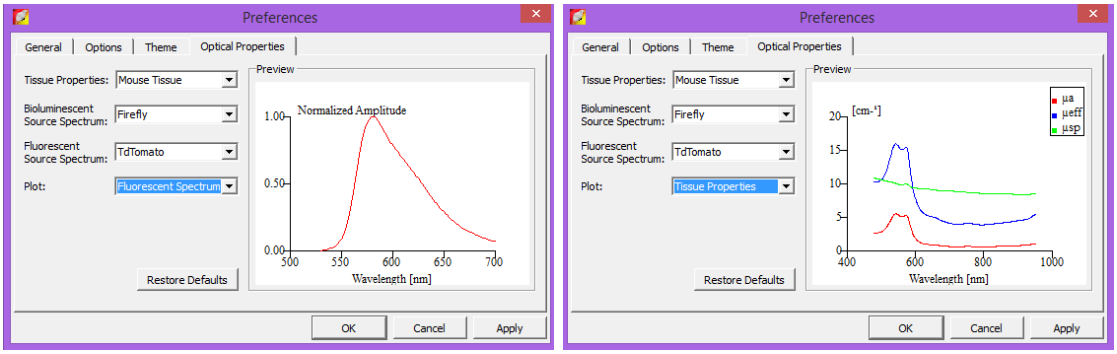

Figure 11: Pre-defined spectra in Living Image software for automatic spectral unmixing; tdTomato spectrum (left), tissue autofluorescence for mouse tissue (right).

In order to separate the fluorescent probe's spectrum from tissue autofluorescence spectrum in in-vivo images, a combination of manual spectral unmixing method with

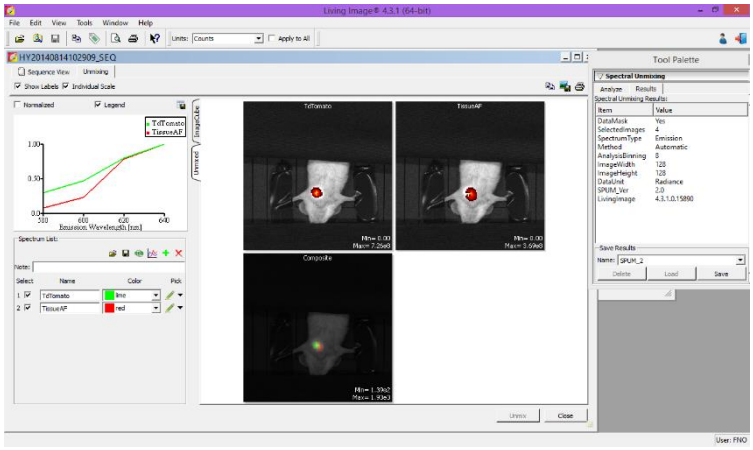

Figure 12: Automatic spectral unmixing results for tdTomato and tissue autofluorescence.

library spectral unmixing was used. The first step was to build a library for tissue autofluorescence spectrum from vector control animals that do not have any fluorescent probes. By selecting the manual spectral unmixing method from the drop-down list, the image cube shows a pseudo color image that is a composite of the stack images that have been colorized to encode spectral information. By moving the mouse pointer over the image cube, the spectrum of a particular location can be observed on the screen. The region of interest that represents the signal location was selected (figure 13), and the measured signal was saved as the tissue autofluorescence library.

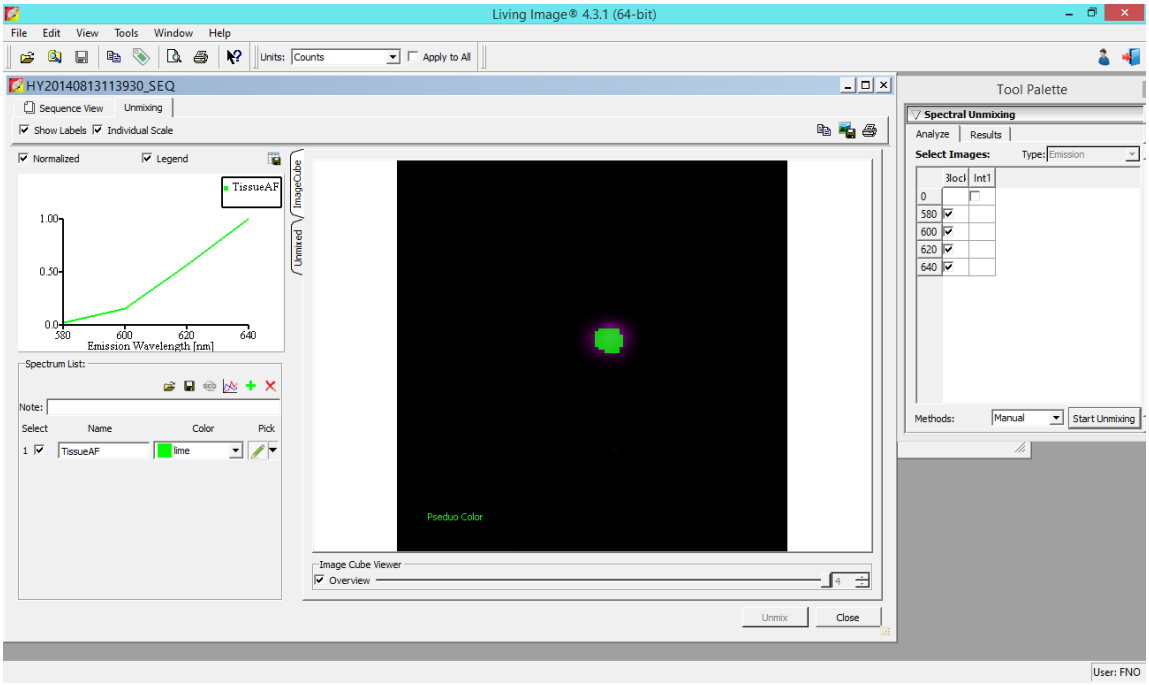

Figure 13: Manual spectral unmixing method to define a library for tissue autofluorescence spectrum using Living Image software.

The fluorescent probe spectrum can be obtained from the infected animals with tdTomato using the same manual spectral unmixing technique. However, the measured signal is an overlap of tissue autofluorescence spectrum and fluorophore's spectrum. In order to correct the overlapping signal, the tissue autofluorescence spectrum was subtracted from the overlapped signal using the Living Image software (figure 14).

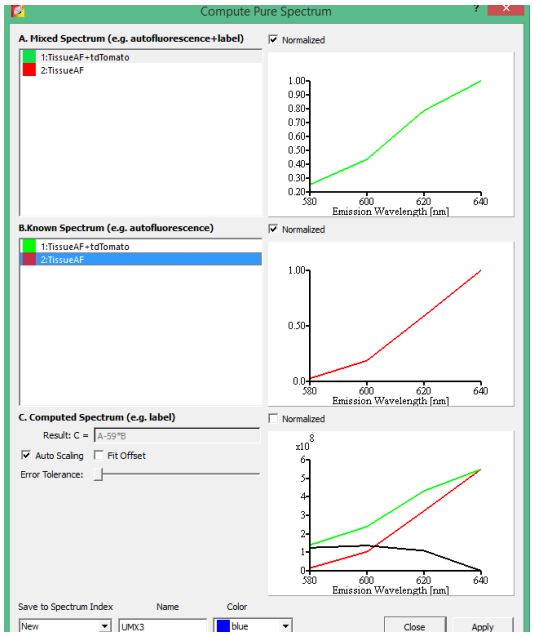

Figure 14: Correction for overlapping spectra by subtracting one spectrum from another in manual spectral unmixing method.

After correcting the overlapped spectra, the spectral unmixing results are shown in figure 15. The calculated spectra for tdTomato and tissue autofluorescence are close to the expected spectra.

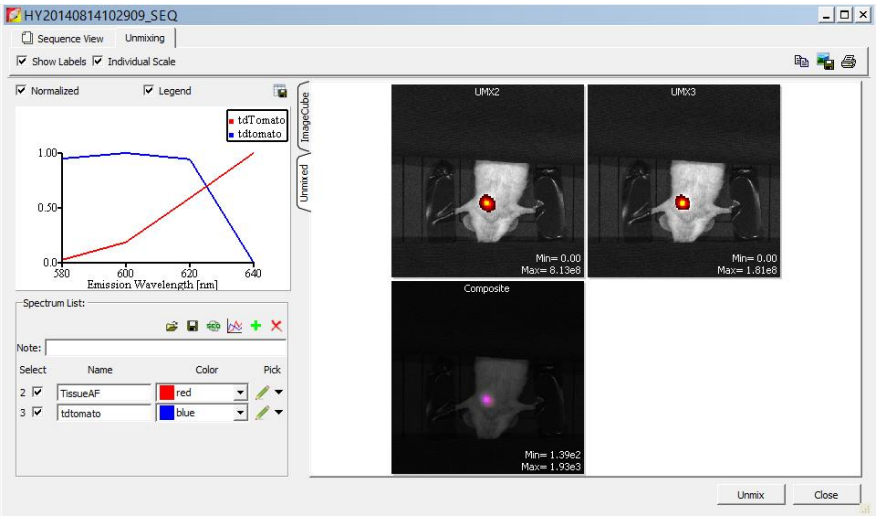

Figure 15: Manual spectral unmixing results following overlapping spectra correction.

4.4 Results

4.4.1 Comparison of intravital excitation using diffusing fiber and multimode fiber

A preliminary evaluation and comparison between the excitation efficiency of the fiber diffuser excitation source and multimode fiber excitation source was performed. Four uninfected mice were imaged first using two intravital excitation sources at tdTomato wavelength's imaging setting. After imaging uninfected animals, the same four mice were infected with 10^6 CFU tdTomato-expressing BCG and imaged 24 hours after infection. IVIS acquisition was performed with the excitation filter set to "block" and the emission filter set to 580, 600, 620, 640 and 660 nm, as well as "open" for imaging the tdTomato-expressing bacteria. The open position was used to determine the location of the tip of the fiber inside the animal. The exposure time for each wavelength was set to "auto". Each animal was also imaged using IVIS excitation (epi-illumination) as well. Figure 16 shows

a representative image of tdTomato-expressing BCG infected mice using the diffusing fiber excitation source [figure 16 (A)] and multimode fiber excitation source [figure 16 (B)] for the same fiber output power (~300 μW). Figure 17 shows mean and standard deviation for infected groups imaged with the diffusing fiber source and multimode fiber excitation source. The results demonstrated that the diffusing fiber excitation source can illuminate larger area of tissue, and enhance the level of the detected fluorescence signal from the tissue.

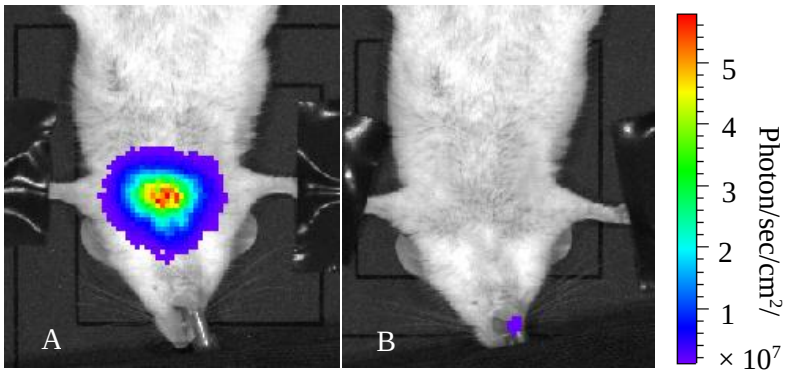

Figure 166: Comparison of excitation efficiency for diffusing fiber excitation source (A) and multimode fiber excitation source (B) for the same output power.

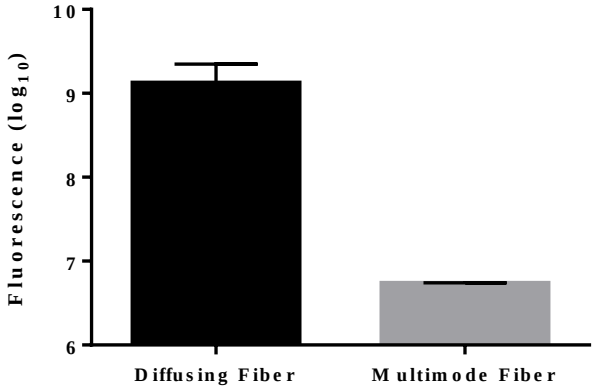

Figure 177: Bar plot of average fluorescence intensity in mice infected by tdTomato-expressing BCG and imaged using intravital fiber excitation source using two different fibers. Error bar shows one standard deviation from the mean.

4.4.2 Comparison of intravital excitation source using diffusing fiber and fiber bundle

Although the excitation efficiency can be improved by adding a diffusing tip at the end of the optical fiber, collecting the fluorescence light emitted from the tissue using the same fiber used for microendoscopic imaging as feedback is not possible using the current diffusing fiber probe. A similar experiment to the diffusing fiber and multimode fiber experiment in 4.2.3 has been performed to compare the diffusing fiber and fiber bundle excitation efficiency. Figure 18 shows the mean and standard deviation for infected groups imaged by diffusing fiber source and fiber bundle.

In figure 18, the average of detected fluorescence intensity is higher for infected groups imaged using the diffuser fiber than the groups imaged using the imaging fiber bundle, but they are not significantly different. Although the diffusing fiber generated comparable excitation efficiency to the fiber bundle, a single diffusing fiber cannot be used for internal detection of the emission light (neither imaging nor sensing), which can

provide feedback on fiber tip position and placement within the airway. In contrast, the microendoscope can provide internal imaging feedback to guide placement of the fiber tip in contact with the tissue to achieve optimal excitation efficiency. Therefore, the imaging fiber bundle microendoscope was used for the experiments described in the remainder of this dissertation.

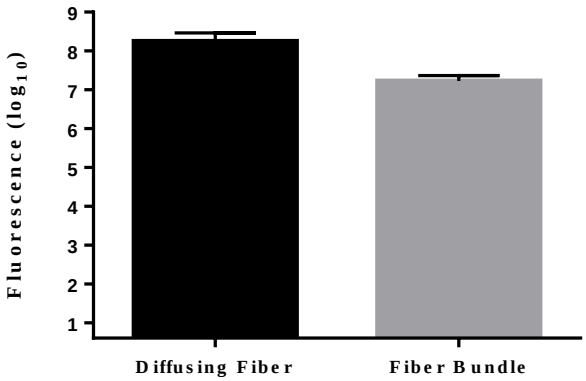

Figure 18: Bar plot of average fluorescence intensity in mice infected by tdTomato-expressing BCG and imaged using intravital fiber excitation source using two different fibers. Error bar shows one standard deviation from the mean.

4.5 Conclusion

In this chapter, the optical design of the intravital fiber-based microendoscope was introduced, and its integration to the whole-animal imaging system was shown. The intravital excitation source was tested using different types of optical fibers, and their imaging performance was evaluated for each optical fiber. Preliminary experiments on

infected animals with 10^6 CFU of BCG17 (tdTomato expressing BCG strain) and 10^5 CFU of BCG39 (empty plasmid) as a negative control revealed that the optical imaging fiber bundle is more suitable for the purposes of this study, since it allows microscopic imaging feedback for bacterial detection. Different techniques for spectral unmixing were compared and their limitations were evaluated. Based on these preliminary experiments, the following studies were designed based on using the imaging fiber bundle as the illumination source, and applying manual spectral unmixing for image analysis.

CHAPTER V

INTRAVITAL FLUORESCENCE EXCITATION TO ENHANCE THE DETECTION SENSITIVITY IN WHOLE-BODY FLUORESCENCE IMAGING OF BACTERIAL INFECTION USING RECOMBINANT STRAINS OF BACTERIA

5.1 Introduction

Whole-animal optical imaging has found widespread use in the biological sciences. Fluorescence-based techniques have been used to study both fixed and live biological specimens, allowing for highly selective and specific detection of molecules even at low concentrations [68]. While traditional fluorescence microscopy requires the sacrifice of multiple animals at discrete time points, whole-animal imaging allows researchers to study disease progression or the efficacy of a therapeutic agent more precisely and with fewer animals than prior imaging techniques [69]. Whole-animal fluorescence imaging is used to study disease pathogenesis, develop novel probes, and measure response to new therapies [41]. Fluorescent reporter strategies include delivery of fluorescent probes targeted to a specific moiety or transfection of cells with genes encoded for a fluorescent protein as an intrinsic reporter probe.

To record a planar image of an internal fluorescent target in a small animal, whole-animal imaging systems can be configured either for epi-illumination, with the light source on the same side of the tissue as the detector, or trans-illumination, with source and detector on opposite sides of the tissue. Although trans-illumination is preferable due to superior tissue volume sampling and reduced skin autofluorescence, trans-illumination

systems are more complex and expensive than epi-illumination. Fluorescence molecular tomography using multiple source and/or detector locations provides enhancements in sensitivity and localization of fluorescent targets over planar trans-illumination [32].

Simplicity in design, ease of operation, and high throughput has yielded broad use of epi-illumination imaging systems, albeit with noteworthy shortcomings. Excitation light is generated from a filtered lamp and broadly distributed over the sample stage to provide relatively even field illumination. Surface and subsurface fluorescence signal emitted from the animal is filtered by high-quality emission filters and captured by a sensitive charge-coupled device (CCD) camera. Epi-illumination systems traditionally suffer from relatively poor depth sensitivity due to light absorption by tissue [41]. Excitation light decreases exponentially with depth; thus, the images are surface-weighted. This is particularly the case when using fluorescent reporters that excite with shorter wavelengths (<600 nm) where hemoglobin absorption is stronger [17]. Additionally, autofluorescence from a wide variety of molecules present in living tissue, particularly the skin in epi-illumination mode, generates significant background signal in this portion of the spectrum [70]. Increased background limits detection sensitivity, especially when the fluorescent target is deep within the animal [71]. Therefore, detected fluorescence signal depends on the brightness and excitation wavelength of the selected fluorescent protein, the number of fluorescent cells, and the depth and location within the animal.

Whole-animal imaging has been used to study a wide range of diseases and organ systems, including brain cancer [72], neurological degenerative disease [73], atherosclerosis [74], myocardial infarction [74, 75], and respiratory infections such as

tuberculosis [44]. For many applications, increased detection sensitivity could greatly enhance the ability to study pathogenesis in more physiologically relevant conditions. For instance, detection of Mtb-expressing tdTomato fluorescent protein has been demonstrated in-vivo for subcutaneous infections of 10^5 CFU [40]. Detection of infections in the lung requires even larger numbers of bacteria, but infections such as these are not physiologically normal, at least at early time points during infection. Thus, significant enhancement of detection sensitivity could improve the ability to study progression of respiratory infection from the onset under more relevant conditions.

Excitation intensities fall off exponentially as light propagates through homogeneous tissue; this loss typically plays a dominant role in detection sensitivity in whole-animal fluorescence imaging. Delivering the excitation light directly to the target area inside of an animal that is placed in a whole-animal imaging system could greatly enhance the ability to measure weak fluorescence signal from deep within the animal.

Fiber-optic based imaging has also become increasingly versatile in recent years as fiber components have decreased in size and gained functionality [76]. Flexible fiber-optic endoscopes, ranging in size of a millimeter up to a centimeter in diameter, have been used to image hollow cavity tissues such as the cervix or digestive tract [20, 52, 77-88]. A fiber-based microendoscope coupled into a whole-animal imaging system allows for excitation light to be delivered inside an animal model. This greatly enhances the intensity inside the animal, as the optical path length between the source and expected location of the fluorophore is minimized. In addition, such a system allows for multi-scale imaging, where microscopic imaging is achieved simultaneously with macroscopic whole-animal

images. Although the use of fiber optic technology can be applied to a variety of biomedical applications where tissue is accessible by a thin optical fiber, the target application for this study is TB, a major public health problem worldwide with a high prevalence in the developing world, where it is the leading cause of death.

TB, caused by Mtb, remains a major global health problem, infecting one-third of the world's population [1]. The slow growth rate of Mtb limits progress toward understanding tuberculosis including diagnosis of infections and evaluation of therapeutic efficacy. There is a growing need for more accurate and rapid diagnostic techniques in order to improve the sensitivity and specificity of the traditional methods for TB detection. A noninvasive biophotonic imaging technique to monitor bacterial dynamics over time with high sensitivity would accelerate pre-clinical evaluation of novel vaccines and therapeutic agents [18]. To significantly enhance detection sensitivity of fluorescent mycobacteria in the mouse lung, we present the integration of an optical fiber into a whole-animal imaging system for intravital excitation of a fluorescent target deep within an animal.

5.2 Methods

5.2.1 Bacterial strains and growth conditions

Mycobacterium bovis BCG is not virulent in humans and is used as a model for tuberculosis in this study, since it is closely related to virulent strains. BCG is an attenuated form of live bovine tuberculosis bacillus and routinely used as a vaccine for TB. However,

BCG retains the ability to infect and persist within mammalian tissue, similar to pathogenic mycobacteria [89]. Two BCG strains, BCG17 (fluorescent protein tdTomato-expressing BCG strain) and BCG39 (BCG strain carrying the same plasmid without tdTomato), were used. Construction of these strains is detailed in [40, 44, 90]. BCG strains were grown in 7H9 broth (Difco, Detroit, MI) supplemented with 0.5% glycerol, 10% OADC (oleic acid dextrose complex without catalase), and 0.05% Tween 80 (M-OADC-TW broth), or on Middlebrook 7H9 (BD, Franklin Lakes, NJ) supplemented with 10% OADC and 15 g/L Bacto agar (M-OADC agar), or on 7H11 selective media (BD).

tdTomato was selected as the fluorescent protein for tuberculosis during infection in mice for reasons described in [91] including its superior quantum yield as compared to the enhanced form of green fluorescent protein (EGFP) [92] and its long emission tail, going out to 700 nm, which makes this protein more suitable for in-vivo imaging [17]. Also, tdTomato has good photostability, which makes it stable throughout imaging with minimal photobleaching [17, 93, 94]. In addition, previous work by Y. Kong et al. demonstrated superior detection limits with tdTomato labeled BCG as opposed to BCG expressing EGFP [40]. Fluorescent systems in microscopy, pathology, and protein analyses are widely used for bacteria and other infectious agents [95-100]. Intravital excitation for whole-animal imaging enhances the potential use of current fluorescent reporters widely used in pre-clinical imaging studies.

5.2.2 Animal infections

All animal experiments in this study were approved by Texas A&M University Institutional Animal Care and Use Committee under animal use protocol number 2015-0222. Five- to seven-week old female BALB/C mice were used in all experiments. Mice were allowed to acclimate to the Biosafety Level 2 (BSL2) facilities for a week and fed AIN-93G diet (Harlan Teklad, Indianapolis, IN; TD.94045), a purified chlorophyll-free diet to reduce background autofluorescence [28, 29, 101, 102], with *ad libitum* access to tap water. Total 42 mice were randomly grouped with six mice in a group. Groups of mice were infected by intratracheal instillation of 10^1-10^6 CFU BCG17 (tdTomato-expressing BCG strain) or 10^5 CFU BCG39 (same plasmid without tdTomato) as a vector control. The detailed procedure of infection was described previously [22]. After 24 hours of infection, whole-body images were acquired using epi-illumination and intravital microendoscope illumination. Mice were sacrificed by injection of 100 µL Fatal-Plus Solution (Vortech Pharmaceuticals Ltd, Dearborn, MI, NDC; 0298-9373-68), and lungs were removed for ex-vivo imaging. The excised lung tissues were homogenized and 10-fold serial dilutions of lung homogenates were plated on 7H11 selective media to enumerate bacterial CFU in the lung.

5.2.3 Fluorescence microendoscope

Figure 19 illustrates the fluorescence microendoscope that was constructed for bacterial detection. The basic design is similar to the system previously reported for the use in bacterial imaging *in situ* [91]. A light emitting diode (Thorlabs, Newton, NJ;

M530L2) centered at 530 nm with a 31 nm bandwidth is used for fluorescence excitation. This wavelength was selected for excitation of tdTomato fluorescent protein (Ex: 554/Em: 581). Light from the diode is collimated, filtered with an excitation filter (Semrock, Rochester, NY; FF01-531/40) and dichroic mirror (Semrock; FF562-Di), and launched into a fiber bundle (Fujikura, Dudley, MA; FIGH-10-500N) by a 10x objective lens (Thorlabs; RMS10X). The 0.66 mm outer diameter fiber bundle consists of 10,000 individual optical fibers. A 3 µm core-to-core spacing limits the resolution, and the 450 µm active area determines the field of view of the microendoscope [103]. Excitation light is guided by the fiber bundle to its distal tip, which can then be inserted into an orifice of an animal model and placed in contact with internal organs. The typical output power from the fiber bundle was measured to be 300 µW. Fluorescence emission incident on the fiber bundle and within its angle of collection is relayed by the bundle, filtered by a longpass emission filter (Semrock; FF01-593/LP-25), and then imaged onto a scientific grade 1.45 megapixel CCD camera (QImaging, Surrey, BC, Canada; EXi Blue) with 6.45 µm x 6.45 µm pixel size.

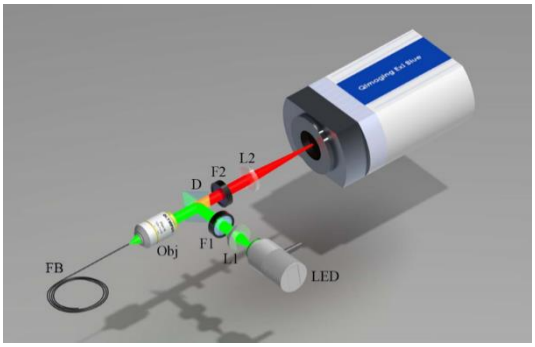

Figure 19: Illustration of the microendoscope system. LED: light emitting diode; L1: collimating lens; F1: excitation filter; D: dichroic beamsplitter; Obj: Microscope objective; F2: Emission filter; L2: focusing lens; FB: fiber bundle [124].

5.2.4 Integration of microendoscope with whole-animal imager

Multi-scale imaging of bacterial infections was achieved by integrating the microendoscope into a whole-animal optical imager (PerkinElmer, Waltham, MA; IVIS Lumina II). The fiber bundle was inserted into the whole-animal enclosure through an access port located on the side of the system, shown in Figure 20. To prevent any external light from entering the system, a 0.5 mm hole was drilled into a rubber stopper (VWR, Radnor, PA; 59580-069) which was then inserted into the access port opening. The fiber bundle was then inserted through the hole in the rubber stopper, as shown in Figure 20 (B).

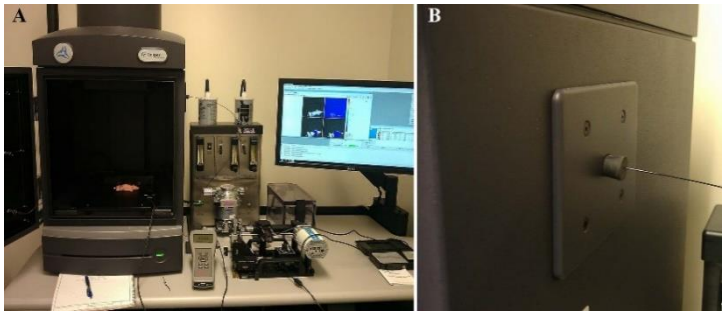

Figure 20: (A) Integration of the intravital fiber excitation source into the IVIS whole-animal imaging system. (B) The fiber is coupled via a test tube stopper placed into the access port of the IVIS system [124].

5.2.5 In-vivo animal whole-body imaging

The detection of respiratory infections of BCG was used to evaluate the enhancement of fluorescence signal in whole-animal imaging using an intravital excitation source. All imaging was performed in a BSL2 laboratory in accordance with local safety regulations. Mouse fur was not removed for imaging; previous work demonstrated accurate localization and detection of tdTomato labeled BCG strains in mice that had fur [40, 44, 90]. A 22G x 1" intratracheal catheter (TERUMO Medical, Somerset, NJ; SURFLO® I.V. SR-OX2225CA) was inserted into the trachea of the mouse anesthetized with ketamine (100 mg/kg) (Henry Schein, Melville, NY) and xylazine (10 mg/kg) (Alfa Aesar, Haverhill, MA) mixture [104]. The mice were then placed on the IVIS stage in a ventral position, and the paws were loosely secured to the stage with tape. The lower abdomen was covered using a black cloth to block background fluorescence signal generated from gastrointestinal tract and kidney. The fiber bundle was inserted into the

intratracheal catheter until it was in proximity with the tracheal wall and fluorescent signal could be observed using the microendoscope. Insertion of the fiber into the mouse airway was limited to the initial bifurcation of the lungs, as guiding the bundle beyond this point is difficult in the small space of a mouse lung. The fiber bundle was marked to ensure comparable insertion distance among animals and to help guide the fiber insertion in the vector control animals. The fiber bundle was also secured to the stage to ensure constant positioning of the fiber during imaging. The distal section of the fiber bundle, which comes in contact with the infected tissue, was thoroughly decontaminated with 70% isopropyl rubbing alcohol (Vi-Jon, Smyrna, TN) after imaging each animal to avoid cross-contamination.

Animal whole-body imaging was acquired by IVIS Lumina II using two different excitation sources – intravital and epi-illumination. First, the microendoscope was used for intravital excitation with the IVIS excitation filter wheel set to 'block' the IVIS illumination. Fluorescence images were collected with the IVIS emission filter set to 580, 600, 620, and 640 nm center wavelengths, as well as the "open" setting, which was used to visualize the illumination profile in the animal. The corresponding microscopic image of the lung tissue was also collected using the microendoscope CCD. Subsequently, the microendoscope source was switched off, and the IVIS excitation filter was set first to 535 nm for excitation of tdTomato fluorescence and then to 465 nm for autofluorescence. Epi-illumination images were captured using the same IVIS emission filter center wavelengths as for intravital excitation. Following whole-body imaging, the lungs were excised and imaged using epi-illumination with the same excitation and emission filter sets as whole-

body imaging. For all images, IVIS acquisition settings were as follows: f/stop: 2, Binning: 8, Automatic exposure.

5.2.6 Image analysis

Manual spectral unmixing was performed using PerkinElmer Living Image software (version 4.3.1) in order to reduce the effects of tissue autofluorescence background and to quantify the tdTomato fluorescence signal detected by whole-body imaging with intravital or epi-illumination. For each animal, the spectrum for tdTomato fluorescence exiting the body from the lungs was estimated by subtracting the spectrum containing both tdTomato and tissue autofluorescence obtained from the mouse infected with tdTomato-expressing BCG strain from the tissue autofluorescence spectrum obtained from the vector control animal. Following spectral unmixing, fluorescence radiance was quantified over a pre-defined region of interest targeting the lungs.

5.2.7 Statistical analysis

Statistical analysis was performed using GraphPad Prism software (Version 6). A nonparametric statistical method, Kruskal-Wallis for multiple comparisons with the Bonferroni posttest (Dunn's procedure), was used to determine statistical significance compared to the vector control [105-107]. $P < 0.05$ was considered significant. To test the correlation of CFU and fluorescence signals, a Pearson correlation test was performed. Linear regression analysis was also applied to determine the relationship between CFU and fluorescence signals.

5.3 Results and discussion

While providing the ability to acquire both macroscopic and microscopic images of bacterial infections from the same animal, the combination of the two optical systems alleviates some of the individual limitations of each. First, the IVIS CCD can be used to localize and track the fiber bundle position inside the animal, allowing for proper positioning of the distal tip prior to data collection. More sophisticated whole-animal imaging systems with optical tomography or x-ray imaging capabilities could allow more accurate determination of the fiber tip location. Additionally, the microendoscope source can serve as an intravital excitation source for the whole-animal fluorescence imager. By delivering the excitation light internally, the attenuation of the excitation light by tissue structures such as the chest wall is greatly decreased, allowing for an increase in the delivery of excitation light inside the region of interest. Prior to in-vivo imaging using intravital excitation, we evaluated intravital excitation illumination in the lung of mouse. Figure 21 (A) shows a mouse with its chest wall opened after sacrifice, exposing the lungs and demonstrating the origin of the intravital excitation light within the animal's body. Figure 21 (B) depicts a typical microendoscope image obtained from the fiber bundle. The fiber bundle pattern is superimposed on the fluorescence signal acquired from the tip of the microendoscope.

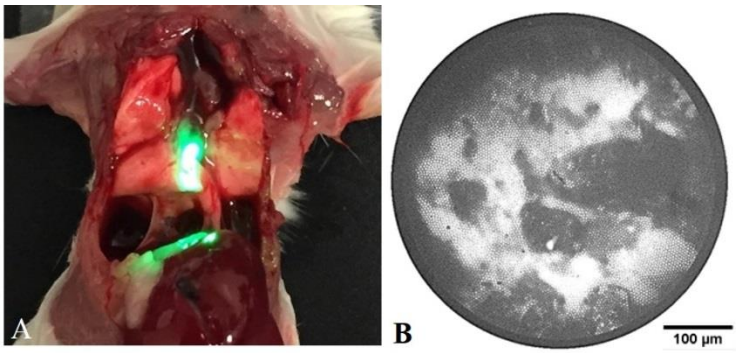

Figure 21: Intravital excitation illumination via microendoscope in the mouse airway. (A) Image of sacrificed mouse with open chest wall and intravital illumination showing the proximal placement of the fiber bundle in the trachea. (B) Example fiber bundle image of BCG17 bacterial fluorescence collected with the microendoscope CCD. The microendoscope image is used to guide placement of the intravital source in contact with tissue prior to IVIS imaging [124].

5.3.1 In-vivo whole-body imaging using intravital fiber excitation

Representative whole-body images acquired using the intravital fiber excitation are shown in Figure 22 (A) for mice infected with 10^1 to 10^6 CFU BCG17, as well as a representative image of a 10^5 CFU infection of BCG vector control. Images with signal levels close to the mean value for the group were considered representative. All images were acquired using identical imaging parameters. Fluorescence images have been scaled such that no signal was present in the vector control for better comparison. Fluorescence signal was quantified by measuring fluorescence intensity over the chest region of interest. Detected fluorescence signal increased with bacterial CFU and minimal signal was observed in the vector control group (Figure 22). We found that intravital excitation could be used to detect pulmonary infection levels of 10^3 CFU with a significant difference from

the vector control ($P < 0.01$). A linear regression fit was applied to assess correlation of the average fluorescence for each group with average CFU in lung homogenates. Fluorescence signal correlates well with bacterial CFU, with $R^2 = 0.945$ ($P = 0.0011$), demonstrating the ability to quantify bacterial CFU using intravital excitation.

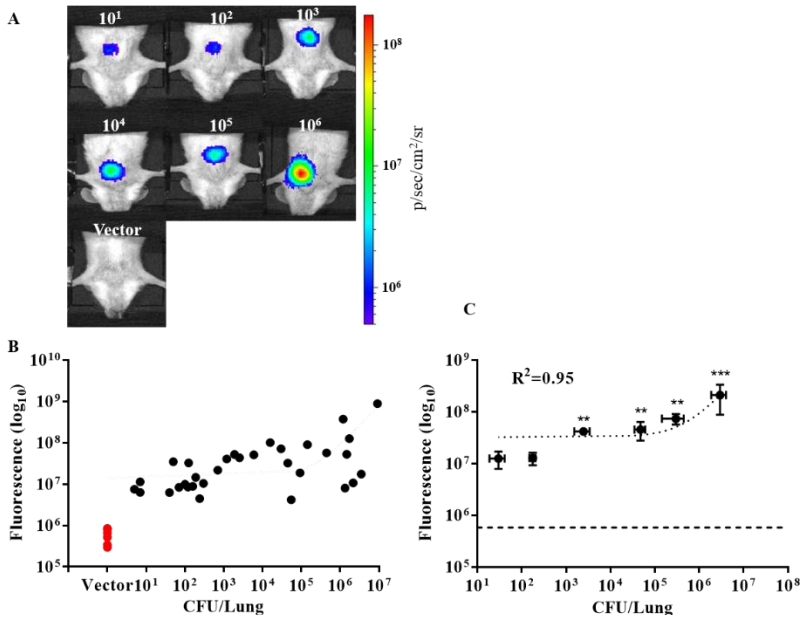

Figure 22: Intravital fluorescence excitation of tdTomato expressing BCG after intratracheal pulmonary infection of mice. (A) Representative whole-body images acquired using integrated microendoscope (intravital fiber excitation) at 24 hr post-infection with 10^1-10^6 colony forming units (CFU) BCG17 and 10^5 CFU BCG39. (B) Scatter plot of fluorescence signal for each animal imaged as compared to actual CFU in lung homogenates from the same mouse. (C) Correlation of fluorescent signal to number of bacterial CFU in lung homogenates. Error bars represent the standard error for each sample group. **p-value < 0.01, ***p-value < 0.001: significantly different from fluorescence of vector control group (horizontal dashed line in C) calculated by non-parametric Kruskal-Wallis test with the Bonferroni posttest. All images and measurements represent tdTomato contribution to signal after spectral unmixing [124].

Representative microscopic images acquired using the microendoscope CCD camera are shown in Figure 23 for the mice infected with different concentrations of BCG17 (10^1-10^6 CFU), as well as a representative image of the 10^5 CFU vector control. Fluorescence signal captured by the microendoscope increased with bacterial numbers, particularly for mice with $>10^4$ CFU in lung homogenates. However, microendoscopic fluorescence is dependent on positioning of the intratracheal catheter and microendoscope fiber tip within the airway. Microendoscope images are primarily used to ensure fiber tip contact with tissue, which results in enhanced intravital excitation for whole-animal imaging. Bacteria are unlikely to be located precisely at the surface of the microendoscope following 24 hr incubation; therefore, spatial variation within a single microendoscope image may be attributed to scattering of fluorescence emission by tissue and mucous structure at the surface of the microendoscope tip.

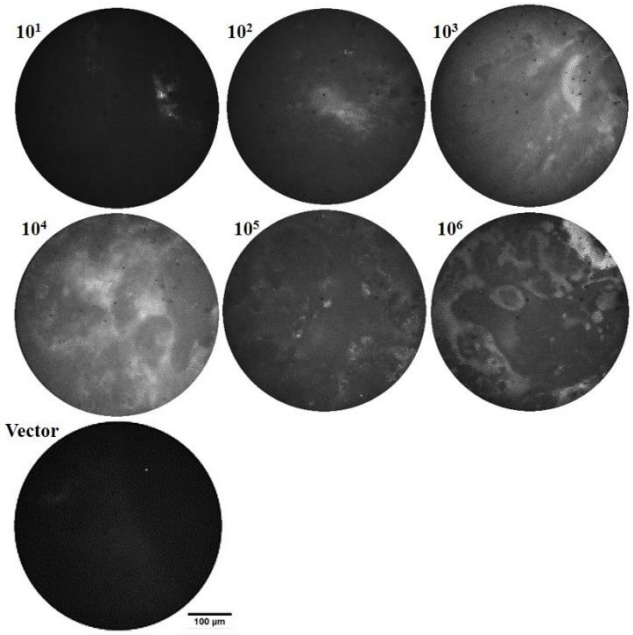

Figure 23: In-vivo microendoscope images provide feedback for positioning the intravital excitation source and can allow a qualitative evaluation of bacterial loads in the lungs. Representative in-vivo fiber microendoscopy images of infected mice lungs, 24 hr post-infection with 10^1-10^6 colony forming units (CFU) BCG17 (tdTomato expressing BCG strain) and 10^5 CFU BCG39 (BCG containing the same vector that does not express tdTomato (Vector)) [124].

5.3.2 In-vivo whole-body imaging using IVIS epi-illumination

To provide a comparison between whole animal imaging using intravital excitation and standard epi-illumination, images were acquired using the IVIS epi-illumination excitation and detection. Representative images for infections of 10^1 to 10^6 CFU BCG17 are shown in Figure 24 (A). A representative image of the 10^5 CFU vector control is shown in Figure 24 (A). Images with signal levels close to the mean value for the group were considered representative. All images were acquired using identical imaging parameters.

Epi-illumination in whole-animal imaging is unable to differentiate between vector control group and infected groups with any statistical significance, even for the highest inoculation dose (P=0.054). Although the fluorescence intensity for BCG17 infected groups is not significantly higher than the vector group, even after spectral unmixing, the detected signal correlates well with CFU numbers. Comparing signal to background levels for epi-illumination (Figure 24 (B)) and intravital illumination (Figure 24 (C)), shows that signal to background level for epi-illumination is less than 2× for all infections; whereas, signal to background level in intravital excitation ranges from 10× to more than 100× with increasing bacterial load.

5.3.3 Ex-vivo lung tissue imaging

To avoid skin autofluorescence and improve penetration of epi-illumination excitation light to the bacteria within the lung, infected lungs were excised and imaged using IVIS epi-illumination. The same acquisition filter settings and manual spectral unmixing method were used as whole-body imaging using IVIS epi-illumination. As shown in figure 25, fluorescence signal correlates with increased bacterial numbers as quantified by CFU in lung homogenates (R^2= 0.851, P=0.0088). However, detection of infection was significant only in the group infected with 10^6 CFU BCG17 as compared to the vector control group (P = 0.0030). Epi-illumination imaging of lungs ex-vivo enhances signal to background compared to in-vivo by the same technique. Internal excitation in excised lungs is not straightforward due to the complexity and small size of the trachea and the potential for collapse of the lungs upon penetration of pleura; however, intravital

excitation combined with whole-animal imaging was found to be more sensitive than ex-vivo epi-illumination.

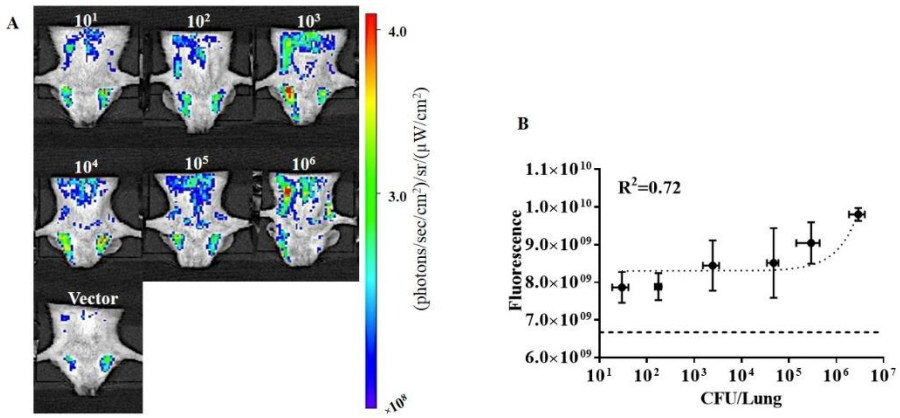

Figure 24: In-vivo whole-body imaging of infected mice using IVIS epi-illumination. (A) Representative images of bacterial infection at 24 hr post-infection with 10^1 to 10^6 colony forming units (CFU) BCG17 (tdTomato expressing BCG strain) and 10^5 CFU BCG39 (BCG containing the same vector that does not express tdTomato (Vector)). (B) Correlation of fluorescence signal in mouse whole-body images versus CFU in lung homogenates from the same animal. Error bars represent the standard error for each sample group. Horizontal dashed line in (B) represents the average signal for the vector control group. All images and measurements represent tdTomato contribution to signal after spectral unmixing [124].

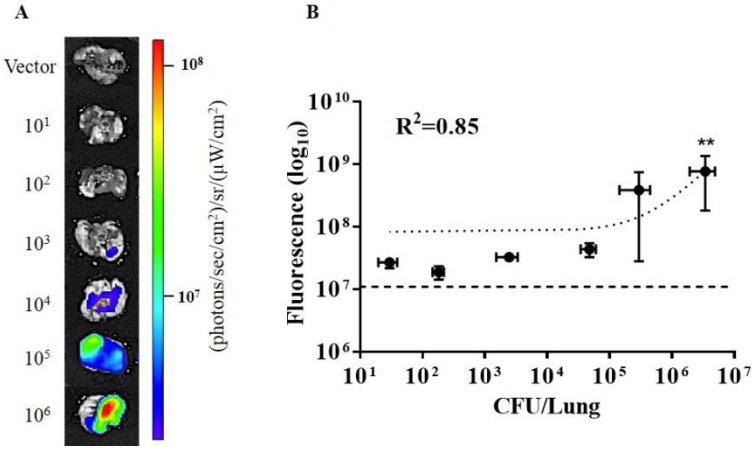

Figure 25: Epi-illumination images of excised mouse lungs infected with tdTomato-expressing BCG or BCG with vector backbone. (A) Representative images of excised lungs infected with 10^1 to 10^6 colony forming units (CFU) BCG17 (tdTomato expressing BCG strain) and 10^5 CFU BCG39 (BCG containing the same vector that does not express tdTomato (Vector)). (B) Correlation of fluorescence signal in ex-vivo images of lungs and CFU in lung homogenates from the same animal. Error bars represent the standard error for each sample group. ** p-value < 0.01: significantly different from fluorescence of vector control group (horizontal dashed line in B) calculated by non-parametric Kruskal-Wallis test with the Bonferroni posttest. All images and measurements represent tdTomato contribution to signal after spectral unmixing [124].

5.4 Conclusions

We have developed a novel system to sensitively detect bacterial infection in living animals. By integrating a fiber-based microendoscope into the IVIS whole-animal imaging system, we enabled intravital excitation of fluorescent bacteria within the mouse lung. Using intravital excitation and whole-animal fluorescence imaging, we decreased the level of detection of tdTomato-expressing bacteria in the lungs of living mice to 10^3 CFU; whereas, epi-illumination for whole-animal imaging was unable to detect infections with as many as 10^6 CFU.

Intravital excitation circumvents the expected absorption of light by the tissue present in the chest wall of mammals. Furthermore, autofluorescence is significantly reduced by illuminating from within the body, similar to the autofluorescence reduction observed with transillumination using whole-body imaging systems. Transillumination, where the light source and detector are located on opposite sides of the animal, provides enhanced detection sensitivity as compared to epi-illumination, most likely due to reflected autofluorescence. As excitation and emission light must be transmitted through the animal to the fluorescent source being detected, these systems inherently are impacted by characteristics of the tissue deep inside the animal and are less affected by the depth of the fluorophore. Therefore, transillumination is more ideally suited for detection of fluorescence from the respiratory system. Intravital excitation has the potential to be more sensitive yet, due to the more direct delivery of excitation light, which is shorter in wavelength than emission light and more dramatically impacted by depth.

While the fiber microendoscope used for these experiments employed a fiber bundle to deliver excitation light to the lungs, a simple large core, multimode fiber could be used in its place. This would allow for additional increases in excitation power delivery. In addition, the system could be further miniaturized and designed to operate solely on battery power. This would allow for imaging inside whole-animal imaging systems that might lack an access port, though this was not necessary for our current system, since the IVIS Lumina II has an access port.

Insertion of the intratracheal catheter and microendoscope into the airway must be performed with great care and caution to avoid tissue damage or animal suffering. There was no evidence of tissue damage due to optical fiber placement. The insertion of an object into the airway has the potential to disturb or artificially spread the infection within the airway. To avoid contamination between animals, the tip of the optical fiber is carefully decontaminated with isopropyl alcohol, after imaging each animal.

A greater understanding of the illumination profile generated within the body by the internal excitation is needed to better understand the physical limitations of intravital excitation. In this study, the fiber bundle excitation source is placed at the tracheal bifurcation and directed towards the base of the lungs. After 24 hours post-infection bacteria may not be present in the trachea or bronchi. Using intravital excitation in mice and other small animals, the highly scattering nature of the lung tissue is exploited to illuminate the entire chest cavity. Excitation light from the intravital source is visible through the chest wall.

Imaging data presented here was acquired 24 hours after bacterial infection. Intravital excitation should be assessed to monitor dynamics of bacterial load over longer time periods. Typically, a granuloma forms at approximately five weeks or later post-infection. The impact of the immune response or granuloma formation on intravital excitation of bacteria within a granuloma would be an interesting avenue of further study, as well as different aspects of pathology that might arise during later stages of disease [108-111].

Beyond the application of this technology to detection of mycobacteria in the lungs, intravital excitation may be applied to enhance sensitivity of fluorescent marker detection in other deep tissues, such as within the gastrointestinal tract. The fiber bundle microendoscope or optical fiber excitation source can be passed through other natural orifices or inserted into the body through a needle in a minimally invasive procedure. We envision a number of additional applications for this technology that could allow improvements in imaging sensitivity of not only infectious diseases, but also other diseases of significant importance that can be evaluated with optical imaging.

CHAPTER VI

IMAGING TUBERCULOSIS WITH ENDOGENOUS B-LACTAMASE

6.1 Introduction

Diagnosis of tuberculosis using standard methods that take weeks to obtain results is a major challenge to control this worldwide disease. Similarly, this bacterial culture timeline limits tuberculosis research using animal models, where data analysis is dependent upon counting of CFU [44]. Although recombinant reporter strains of mycobacteria such as tdTomaro-expressing BCG bacteria have been established to detect mycobacteria in animal experiments using different imaging techniques (fluorescence, luminescence [112-116], single photon emission computed tomography (SPECT) [117, 118]), these techniques need specific laboratory strains or cannot be used for specific detection of pulmonary TB directly in-vivo. Expression of foreign genes in recombinant reporter strains can alter bacterial fitness in unexpected ways, especially when expressed from plasmids [119-121]. Therefore, the development of a non-invasive technique that allows detection of Mtb directly without expression of foreign genes would facilitate TB research with clinical strains, and would have a great impact on developing TB therapeutics and vaccines. The sensitive detection of nonrecombinant strains can ultimately be applied to patients' sputum and other diagnostic samples, as well as patients themselves.

A reporter enzyme fluorescence (REF) system, using a custom synthesized near-infrared (NIR) β-lactamase (BlaC)-specific fluorogenic substrate, CNIR5, has been

developed for real-time imaging of pulmonary infections and quantification of Mtb infection in-vivo. This technology has made a significant breakthrough in the whole animal imaging threshold of detection of bacteria in the lungs of mice, down to ~10^4 CFU, a 100-fold improvement over recombinant strains [44]. However, improvement of detection sensitivity is needed for clinical diagnosis of early stage infection at greater tissue depth. In order to improve detection sensitivity, we have integrated a fiber-based microendoscpe into a whole-animal imaging system to transmit the excitation light from the fiber bundle to the fluorescent target and measure fluorescence using a BlaC-specific REF substrate in the mouse lung.

6.1.2 Imaging with reporter enzyme fluorescence (REF)

Figure 26 (A) shows the expression of β-lactamase enzyme in three common Mtb strains including H37Rv, CDC1551, and Erdman, and H37Rv blaCm strain with a mutation in the blaC gene. As expected, all Mtb strains produce a measurable membrane-localized β-lactamase within 2 hour to 20 hour, as measured by the change in fluorescence of Fluorocillin Green (Ex/Em: 485/530 nm), in the presence of 10^7 bacteria. The significant difference between the fluorescence signal of the mutant H37Rv blaCm and other Mtb strains indicates that BlaC is responsible for the majority of β-lactamase activity in Mtb. Figure 26 (B) shows that Mtb BlaC is primarily surface-localized, makes it an ideal candidate for Mtb detection, since substrates would not need to traverse the highly selective mycobacterial cell wall [44].

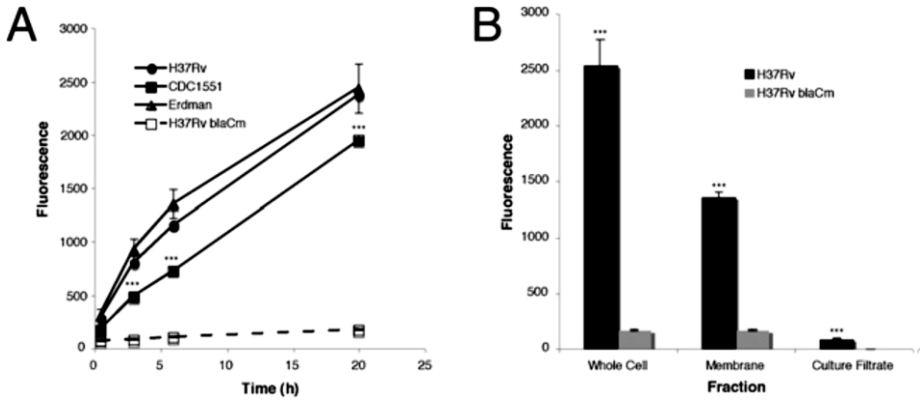

Figure 26: Expression of β-lactamase in different strains of Mtb produce a membrane-localized β-lactamase [45]

Reporter enzyme fluorescence (REF) utilizes β-lactamase (BlaC) enzyme, along with a custom designed fluorogenic substrates. The substrate is composed of a fluorochrome and a quencher that are connected by a β-lactam ring. The custom substrates for REF also carry acetylated D-glucosamine connected to the carboxylate of cysteine through γ-amino-butyric acid producing a charged molecule, which facilitates uptake into eukaryotic cells [122]. Once this substrate is within cells, β-lactamase secreted by intracellular bacteria cleaves the β-lactam ring. Once the β-lactam ring is hydrolyzed by β-lactamase, the fluorochrome moiety is released from the quencher and generates a near infrared fluorescent molecule [123]. This system does not utilize recombinant strains, which has a significant advantage over reporter strategies, since it is unlikely to have unexpected impacts on virulence [119-121]. Figure 27 depicts the REF approach to imaging bacterial infections.

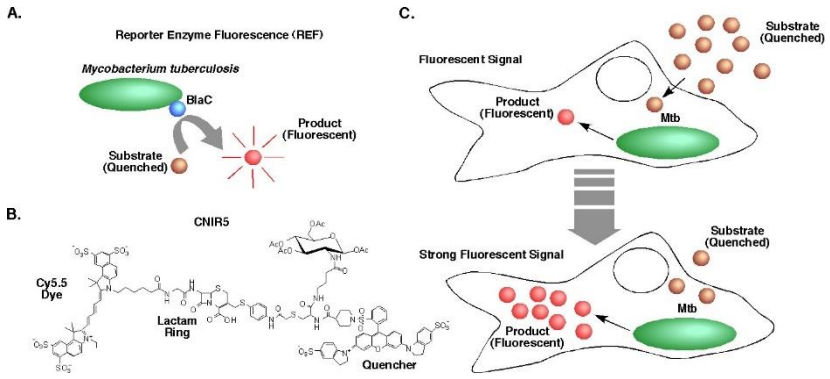

Figure 27: (A) Depiction of REF in Mtb. The substrate that is quenched becomes fluorescent upon cleavage by BlaC, an enzyme located on the surface of Mtb, which prevents the need for the substrate to cross the bacterial cell wall. (B) Structure of the first generation substrate CNIR5 that uses Cy5.5 as the fluorescent dye. (C) Mechanism thought to be involved in amplification of REF signal. Signal builds up in the host cell due to the cleaved, fluorescent dye binding to molecules in the host cell. Fluorescent signal can reach very high levels at the site of infection by building up in the host cell [45].

The extremely high sensitivity of REF in whole-animal imaging is most likely due to the catalytic nature of the reporter (BlaC) and the ability of cleaved, fluorescent products to build up in the host cell. The resulting fluorescence characteristics would be similar to the characteristic of the flourogenic dye used to make the custom substrate [123]. To detect Mtb using BlaC, several NIR substrates have been developed with a long wavelength fluorescent signal when cleaved (figure 28 (A)), making them good candidates for use in

in-vivo animal imaging, because of their ability to penetrate efficiently in animal tissue. All these substrates show little fluorescence signal before their BlaC cleavage and increase in maximal emission after cleavage (figure 28 (B)). Incubation of each of these probes with Mtb resulted in an increase in fluorescence signal (figure 29) [44].

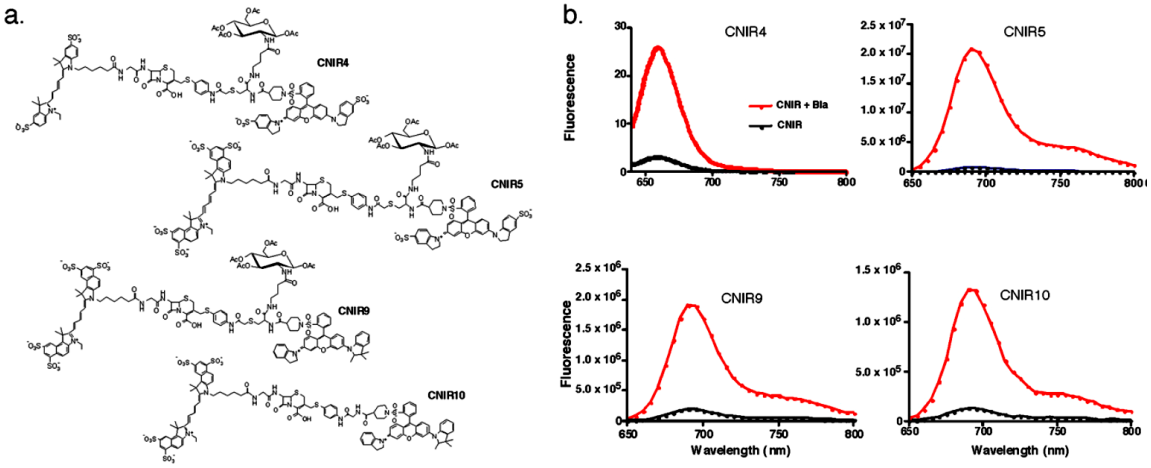

Figure 298: (A) Structure of CNIR substrates. (B) Fluorescence emission spectra of each CNIR substrates before and after BlaC cleavage [45]

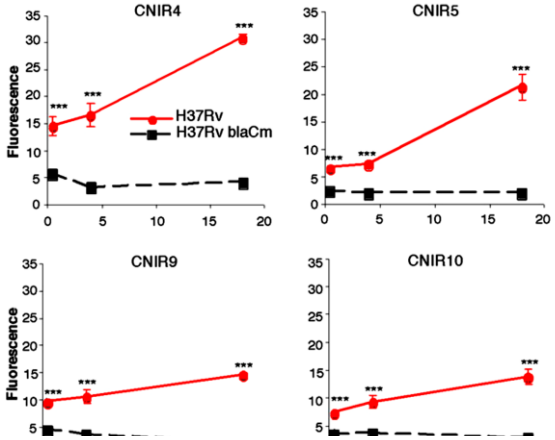

Figure 289: Kinetics of CNIR substrates incorporation into Mtb and Mtb blaC mutant (blaCm) [45]

The substrate CNIR5 has been used for detection and quantification of Mtb in-vitro and in-vivo, since it shows an improved increase in fluorescence signal after incorporation into Mtb. The in-vitro results show a good correlation between bacterial CFU numbers and level of fluorescence signal for bacterial range of 10^2 to 10^6 CFU (figure 30 (A)). Real-time analysis of Mtb in living mice using CNIR substrates shows that CNIR5 could detect 10^6 bacteria, however the other CNIR substrates could detect 10^7 CFU. The highest fluorescence signal was observed at 48 hour post-administration of CNIR5, followed by CNIR10, CNIR4, and CNIR9 for animals infected with Mtb and closely related vaccine BCG (figure 30 (B-C)). The charged nature of Cy5.5 causes it to bind to lipids or proteins present in the host cell and be retained for extended periods of time, which can be as long as 72 hour post-administration of the substrate [44].

In this study, we used the intravital fiber optic fluorescence microendoscope integrated into a whole-animal imaging system for tuberculosis detection in-vivo using a NIR BlaC-specific fluorogenic substrate, CNIR800. We demonstrated that integration of these optical imaging technologies with BlaC-specific fluorescent reporter probes can enable sensitive detection of bacteria in lungs of living animals. This technology can also improve the sensitivity of whole-animal optical imaging to enable study of early stage bacterial infection, evaluation of therapeutic efficacy, and development of preventative treatments.

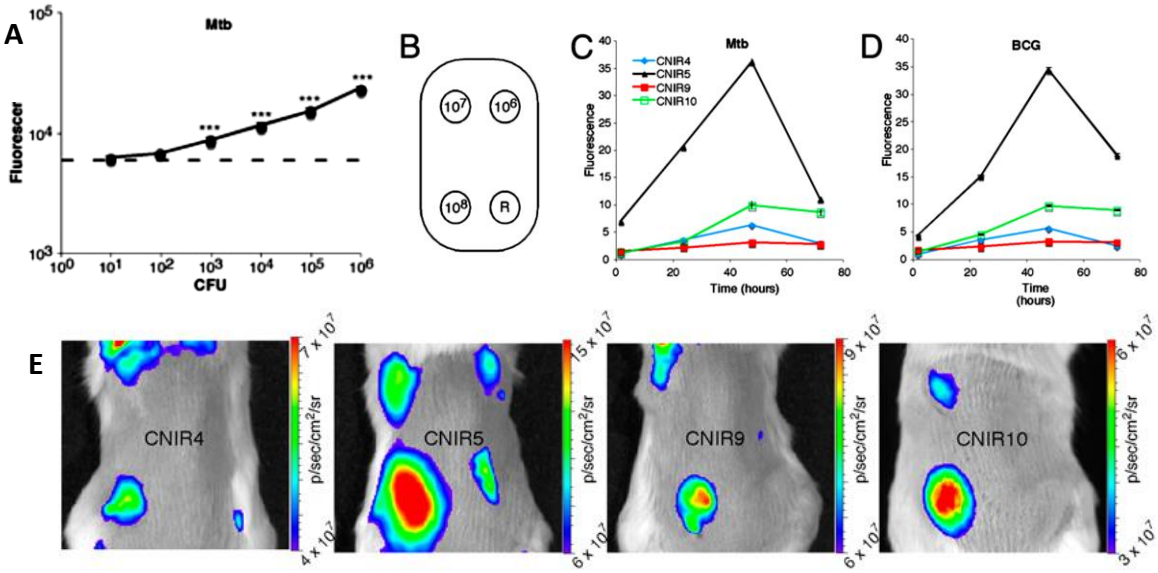

Figure 30: (A) Correlation of fluorescence signal Mtb bacterial CFU numbers in the presence of CNIR5 for 24 hour in-vitro. (B) Inoculation sites for different CFU numbers in in-vivo experiments along with the position of the reference measurement (R). (C) Comparison of the fluorescence signal over time for each CNIR substrate for 10^8 Mtb and (D) BCG. (E) Whole-animal imaging of mice infected with Mtb and administrated CNIR substrates at 48 hour post-infection and post-administration [45].

6.2 Methods

6.2.1 Animal infection

Mice were randomly grouped in six groups of four mice per group. The mice were anesthetized and infected with 10-10^6 CFU of *M. bovis* BCG strain by intratracheal instillation. *M. bovis* BCG strain was used in this study as a safety precaution because it is closely related to *M. tuberculosis* but not virulent in humans [89]. A detailed protocol for the method of infection was described previously [22]. 24 hours after inoculation, the

mice were imaged using the whole-body imaging system with intravital excitation. Following imaging, the lungs were excised, homogenized, and 10-fold serial dilutions of lung homogenates were plated on 7H11 selective media for culturing and CFU counting.

Animal use protocols were approved by the Texas A&M University Institutional Animal Care and Use Committee. Five- to seven-week old female BALB/C mice were used in this study. Mice were fed alfalfa-free AIN-93G diet with *ad libitum* access to water. A mixture of ketamine (100 mg/kg) and xylazine (10 mg/kg) was used for anesthesia.

6.2.1 Reporter enzyme fluorescence technology and substrate CNIR800

The CNIR800 substrate consists of IRDye 800CW fluorescent dye linked to a quencher (IRDye QC-1) at the distal end through a lactam ring, providing a fluorescence resonance energy transfer (FRET) quenching effect (Figure 31) [123]. In the absence of BlaC (no mycobacteria), the substrate is quenched and produces minimal fluorescence. BlaC cleavage of the lactam ring releases the quencher from CNIR800, significantly increasing fluorescence of the IRDye. Cleaved CNIR800 displays maximal signal at an emission wavelength of 795 nm with 745 nm peak excitation. The CNIR800 REF substrate (20 μM, 2.5 μl/g of weight) was administered intratracheally at 24 hours post-infection.

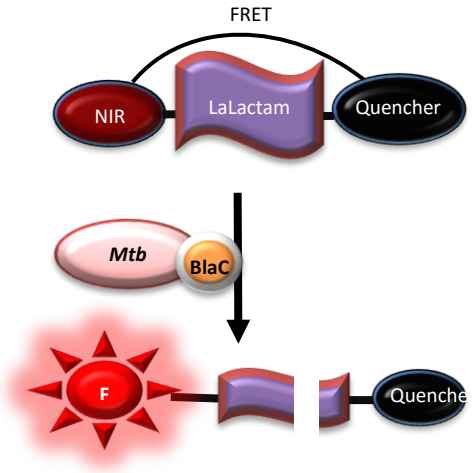

Figure 31: Schematic representation of the reporter enzyme fluorescence (REF). The β-lactamase enzyme naturally and constitutively expressed in *Mycobacterium tuberculosis* is used to cleave the lactam ring, releasing the FRET quencher and allowing recovery of the IRDye 800CW fluorescence

6.2.2 Whole-body fluorescence imaging system with intravital excitation

Figure 32 shows the integrated whole-body imaging system with intravital excitation used in this study, previously described in detail [124]. The fiber-based microendoscope image provides real-time feedback for guidance of placement of the fiber bundle tip within the airway. In tandem, the microendoscope excitation within the airway serves as the intravital light source for whole-body imaging with the IVIS illumination blocked.

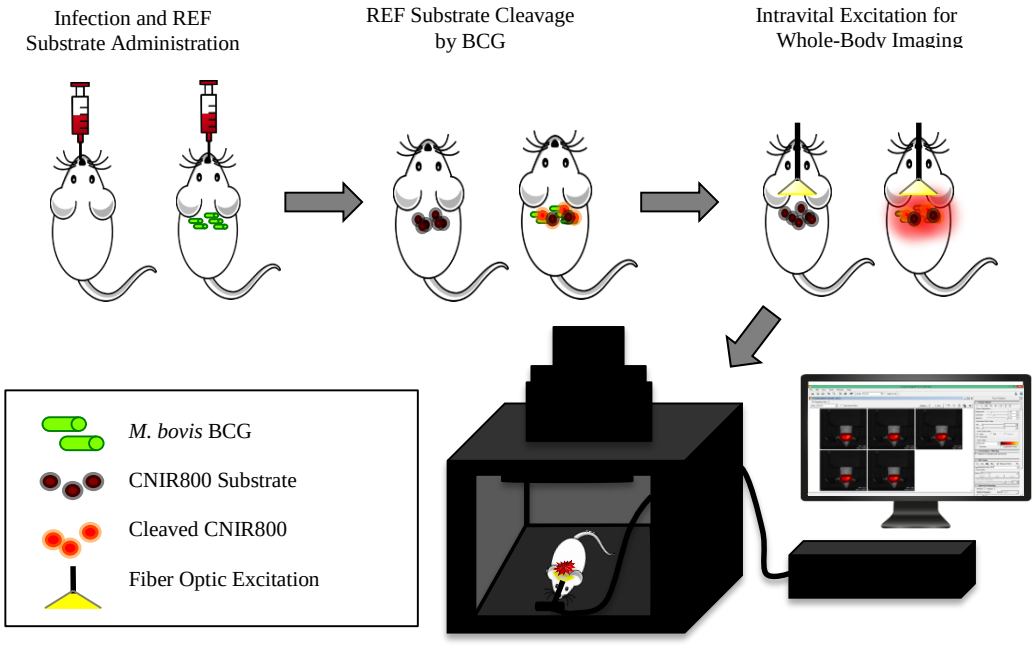

Figure 32: Whole-body imaging of REF fluorescence with intravital excitation in the airway of live mice. 24 hours after BCG infection via intratracheal instillation, CNIR800 REF substrate is administered through an intratracheal catheter. After a time period to allow CNIR800 cleavage, mice are placed in the whole-body imaging system and the microendoscope is inserted into the airway for intravital excitation and whole-body imaging.

The 10,000-fiber bundle (FIGH-10-500N, Fujikura) is routed through an access port into the whole-body imaging system (IVIS Lumina II, PerkinElmer), enabling insertion into the trachea of the anesthetized mouse through a 22G x 1” catheter (SURFLO® I.V. SR-OX2225CA, TERUMO Medical). The excitation pathway of the microendoscope consists of a 730 nm laser diode (HL7302MG, Thorlabs), excitation filter with 750 nm cut-off wavelength (FES0750, Thorlabs), and 757 nm dichroic mirror (FF757-Di01, Semrock) targeting fluorescence excitation of the CNIR800 REF probe. A

10× objective lens (RMS10X, Thorlabs) couples the illumination and imaging system to the fiber bundle. A 776 nm emission filter (FF01-776-LP, Semrock) passes CNIR800 fluorescence to a 1.45 megapixel CCD camera (EXi Blue, QImaging). The microendoscope fiber bundle has 0.66 mm outer diameter, 3 μm core-to-core spacing, and 450 μm field of view [91]. Output power from the fiber bundle was measured to be 1.2 mW.

6.2.3 In-vivo animal whole-body imaging using REF technology

Whole-body images of mice were acquired using both intravital fiber excitation and IVIS epi-illumination at various time points post-administration of CNIR800. After whole-body imaging, animals were sacrificed and lung homogenates were plated for CFU counting. To collect images with intravital fiber excitation, a catheter was inserted into the trachea of the animal, and the animal was placed on the IVIS stage in the ventral or dorsal position. The lower torso of the mouse was covered with a black cloth to block background fluorescence of the gastrointestinal tract and kidney. The fiber bundle was fed into the catheter until it was in contact with the airway wall. The fiber position was guided and confirmed with the image on the CCD camera of the microendoscope. The fiber bundle was then marked at the mouth to ensure comparable insertion distance among animals and secured to the stage to prevent movement during stage height adjustment for imaging.

The excitation light source from the IVIS system was blocked, and IVIS fluorescence emission filters were selected to collect CNIR800 signal at20-nm increments from 760 to 840 nm using the IVIS camera. After imaging with intravital excitation, epi-

illumination images of the same animal with the IVIS imaging system excitation source were collected for comparison. Epi-illumination excitation filters of 675 nm and 745 nm were used for background tissue autofluorescence and CNIR800, respectively. The same IVIS emission filter settings were used as the intravital fiber excitation configuration. Each acquisition was taken with an f-stop of 2, medium binning, and automatic exposure settings.

Manual spectral unmixing was performed using PerkinElmer Living Image software (version 4.3.1) to reduce tissue autofluorescence background and quantify the REF signal detected by whole-body imaging with intravital or epi-illumination. Following spectral unmixing, fluorescence radiance was quantified over a pre-defined region of interest targeting the lungs.

Statistical analyses were performed using GraphPad Prism software (Version 6). Student's two-tailed t-test was used to determine statistical significance compared to the control; $P < 0.05$ was considered significant. Pearson correlation was used to test the correlation of CFU and fluorescence signals. The relationship between CFU and fluorescence signal was determined using a linear regression analysis.

6.3 Results

6.3.1 Peak CNIR800 substrate fluorescence signal at 4 hours post-pulmonary administration

At 24 hours post-infection, CNIR800 was delivered by aerosol to mice carrying 10^6 CFU of *M. bovis* BCG in the lungs to evaluate the kinetics of the REF substrate

CNIR800 to detect bacterial infection in the mouse lung. Pulmonary delivery of substrates improves the signal-to-noise ratio (SNR) by concentrating delivery to the target infection site and decreasing background signal from other organs and tissues that could otherwise accumulate substrate. Intravital excitation with whole-body imaging was performed every 2 hours over a 12 hour period (Figure 33 A). In-vivo fluorescence signal from the cleaved substrate significantly increased 2 hours post-administration of the substrate with the maximum fluorescence at 4 hours (Figure 33 B). Fluorescence signal in the infected animal at 8 hours post-administration was not significantly different than the 0 hour timepoint, suggesting that the ideal window for imaging by pulmonary delivery of CNIR800 is between 2 and 6 hours post-administration of the substrate. Aerosol delivery into the airway showed more rapid kinetics than intraperitoneal (IP) delivery of the substrate, which had a gradual signal increase from 2 hours until it reached a maximum at 6 hours post-administration (Figure 33 C).

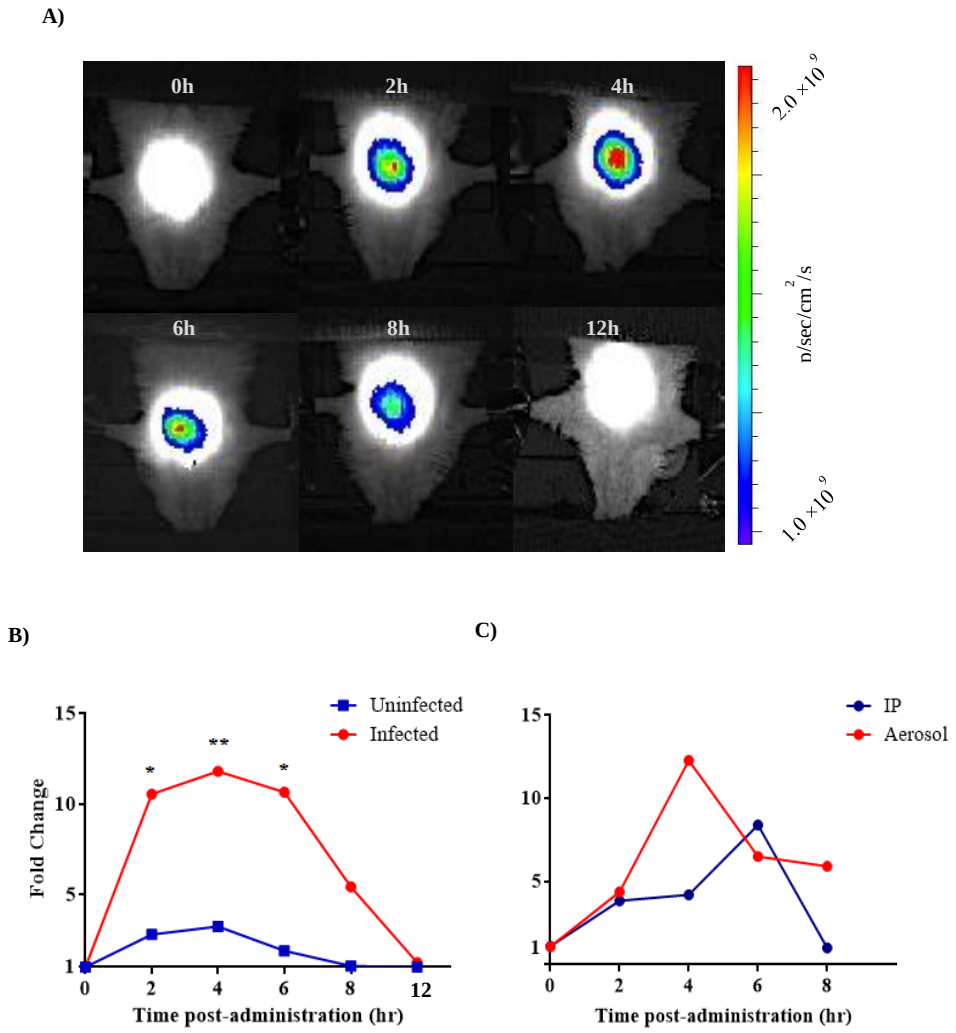

Figure 33: Kinetics of aerosol delivery of CNIR800 (20 µM, 2.5 µl/g) in mice infected with 10^6 CFU *M. bovis* BCG strain in the lungs. (A) Representative whole-body images acquired with intravital excitation at time points post administration of CNIR800. (B) Comparison of fluorescence signal fold change over signal at initial time point for infected and uninfected mice. *p-value < 0.05, **p-value < 0.01: significantly different from fluorescence signal at 0 hour using Student's two-tailed t-test. (C) Comparison of kinetics of aerosol delivery and IP delivery of CNIR800

6.3.2 Dorsal position exhibits the highest SNR at 4 hours post-administration of CNIR800

Groups of mice infected with 10^6 CFU *M. bovis* BCG were imaged at 2 and 4 hours post-administration of CNIR800 in dorsal and ventral positions on the IVIS stage. SNR was calculated at each time point by dividing fluorescence signal detected in infected mice by the signal in uninfected mice for each position (Figure 34 C). At 2 hours post-administration, both positions exhibited a similar SNR. However, at 4 hours post-administration, SNR was significantly increased in dorsal position as compared to the ventral position despite the fluorescence signal being higher in the ventral position. The SNR of the images in the dorsal position at 4 hours post-administration was also significantly higher than the same position at 2 hours post-administration ($P = 0.029$).

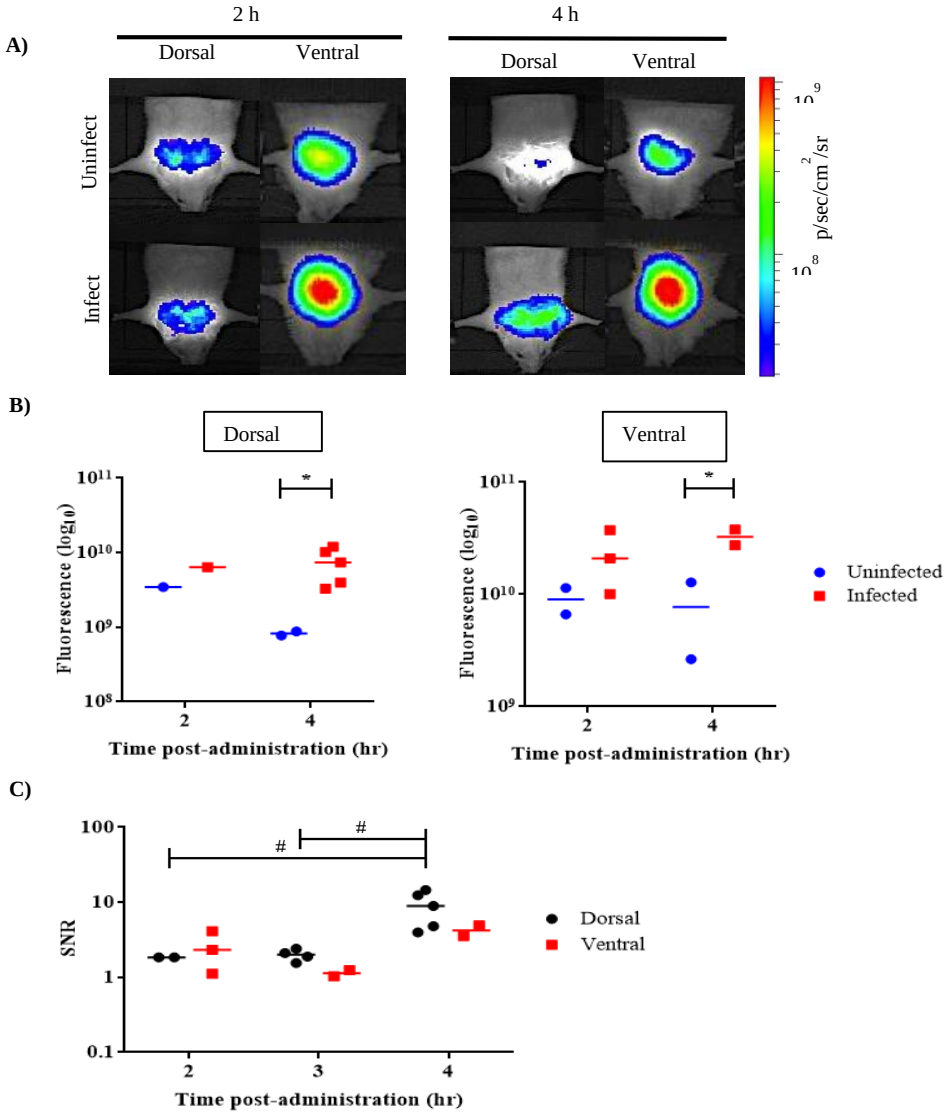

Figure 34: Effect of animal positioning on fluorescence detection and signal to noise ratio (SNR) in whole-body imaging with intravital excitation. (A) Representative images of mice in ventral or dorsal position acquired at 2 hours and 4 hours post-administration of CNIR800. Comparison of (B) fluorescence signal and (C) SNR (fluorescence signal in infected animals normalized to signal in uninfected animals) in different animal positions at different times post-administration of CNIR800. *p-value<0.05: significantly different from fluorescence of uninfected control group calculated by Student's t-test; +p-value<0.05, ++p-value<0.01: significantly different in fluorescence among different imaging time points calculated by two-way ANOVA.

6.3.3 Detecting pulmonary infection in mice using BlaC-specific substrate

Six groups of mice were infected with 10^1-10^6 CFU of *M. bovis* BCG intratracheally, and CNIR800 was delivered to the mice via aerosol at 24 hours post-infection. Mice were first imaged using intravital fiber-optic excitation 4 hours post-administration of the substrate. Immediately after, mice were imaged using epi-illumination of whole-body imaging system (IVIS Lumina II) for parallel comparison of these systems. As shown in Figure 35, whole-body imaging with intravital fiber-optic excitation using CNIR800 provided a threshold of detection as low as ~100 CFU in the mouse lung (Figure 6.10C; P = 0.029). Fluorescence signals correlated with the number of bacteria present in the mouse lung to 100 CFU (Figure 35 C; R^2 = 0.95, P = 0.0008), while epi-illumination of the animal only allowed detection of 10^4 CFU (Figure 36 C, R^2 = 0.36, P = 0.211). Imaging using intravital fiber-optic excitation improved the threshold of detection over epi-illumination by ~100 fold.

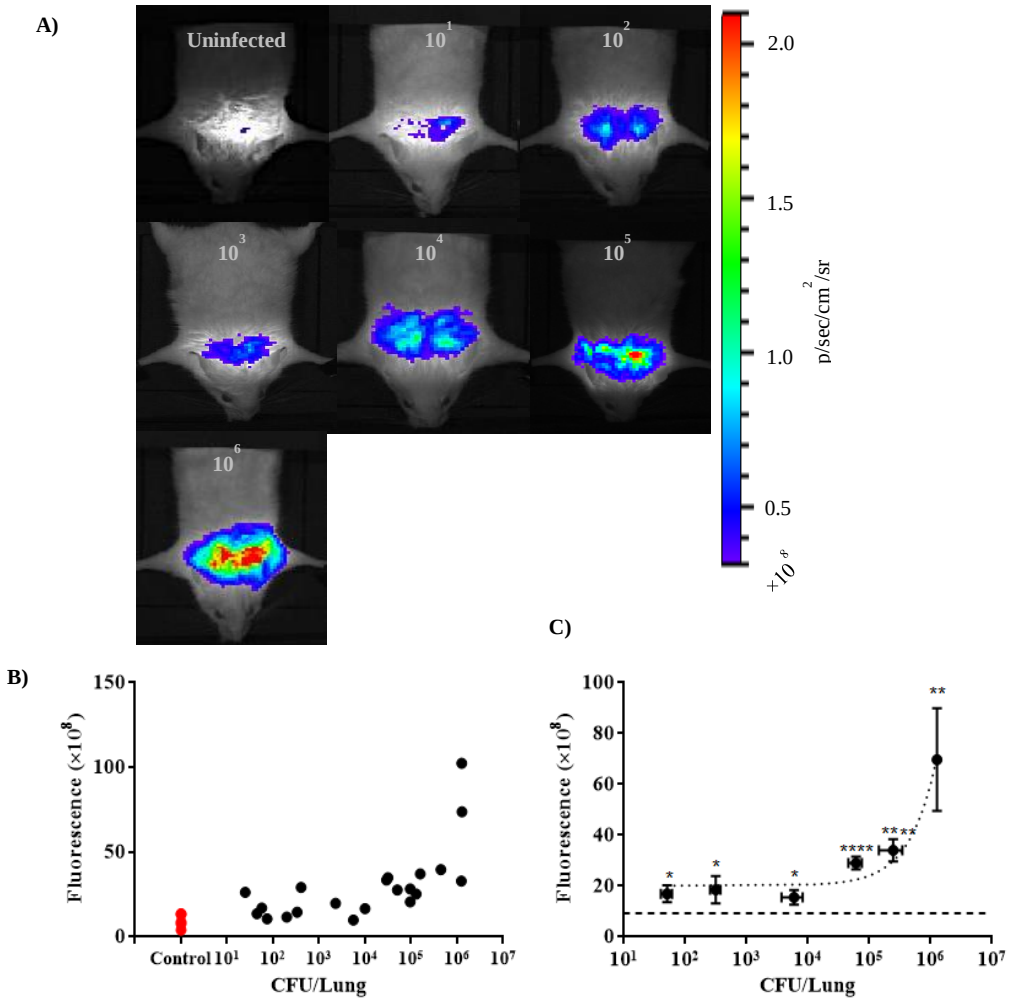

Figure 35: Whole-body imaging using intravital fiber excitation of mice infected with 10-10^6 CFU *M. bovis* BCG strain and labeled with REF substrate CNIR800 delivered intratracheally 24 hours post-infection. (A) Representative images 4 hours post-administration of CNIR800. (B) Scatter plot of fluorescence signal for each animal as compared to actual CFU obtained from lung homogenates of same animal. Each dot denotes an individual animal. R^2 was calculated using linear regression. (C) Fluorescence versus grouped CFU from lung homogenates. Bars represent average fluorescence of each group and error bars denote standard error. *p < 0.05, **p < 0.01, ***p < 0.001, ****p < 0.0001: significantly different as compared to the fluorescence in uninfected group, calculated by Student's two-tailed t-test.

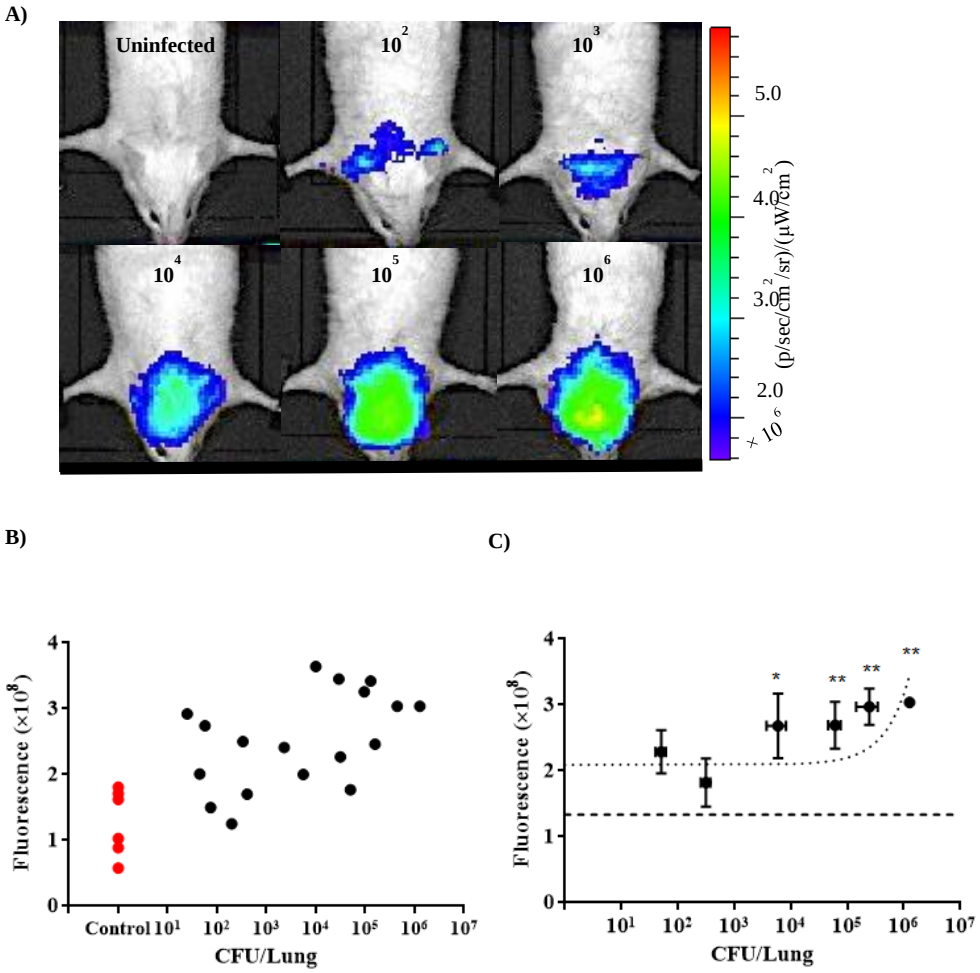

Figure 36: Whole-body imaging using IVIS epi-illumination of mice infected with 10-10^6 CFU M. bovis BCG strain and labeled with REF substrate CNIR800 delivered intratracheally 24 hours post-infection. (A) Representative images 4 hours post-administration of CNIR800. (B) Scatter plot of fluorescence signal for each animal as compared to actual CFU obtained from lung homogenates of same animal. R2 was calculated using linear regression. (C) Fluorescence versus grouped CFU from lung homogenates. Bars represent average fluorescence of each group and error bars denote standard error. *$p < 0.05$, **$p < 0.01$: significantly different as compared to the fluorescence in uninfected group, calculated by Student's two-tailed t-test.

6.3.4 Detecting recombinant strains of bacteria vs. non-recombinant strains of bacteria using intravital illumination

Figure 37 shows the scatter plot of fluorescence signal imaged by whole-body imaging using intravital fiber excitation of mice intratracheally infected with 10-10^6 CFU of tdTomato expressing BCG *M. bovis* bacteria (Figure 37 A) and 10-10^6 CFU *M. bovis* BCG strain and labeled with REF substrate CNIR800 (Figure 37 B) 24 hours post-infection.

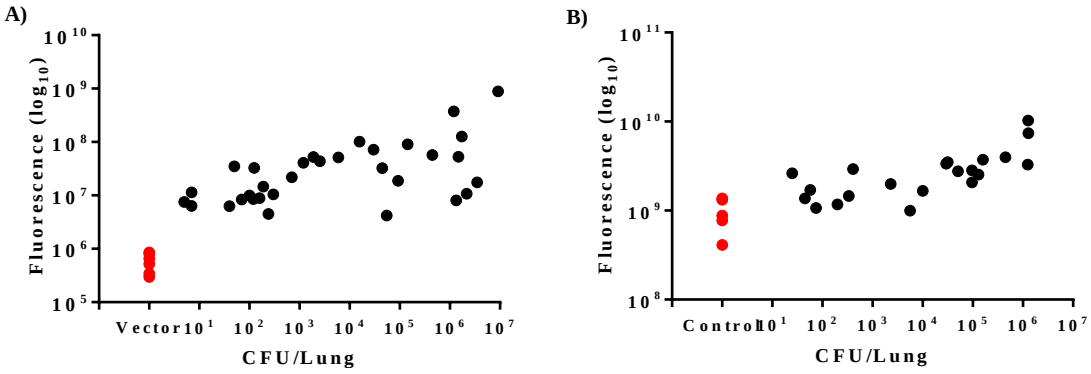

Figure 37: Scatter plot of fluorescence signal for each animal infected with (A) tdTomato expressing *M. bovis* BCG and (B) *M. bovis* BCG labeled with REF substrate CNIR800 as compared to actual CFU obtained from lung homogenates of same animal. Each dot denotes an individual animal

As shown in Figure 38, whole-body imaging with intravital fiber-optic excitation using either recombinant strains of bacteria (tdTomato-expressing *M. bovis* BCG) or non-recombinant strains of bacteria (BlaC-specific substrate) provided a threshold of detection

as low as ~100 CFU in the mouse lung using the parametric Student's t-test (P = 0.026, P = 0.029, respectively). Also, a nonparametric statistical method, Kruskal-Wallis for multiple comparisons with the Bonferroni posttest (Dunn's procedure), provided a threshold of detection ~ 10^3 CFU for both recombinant and non-recombinant strains of bacteria (P = 0.002, P = 0.04, respectively).

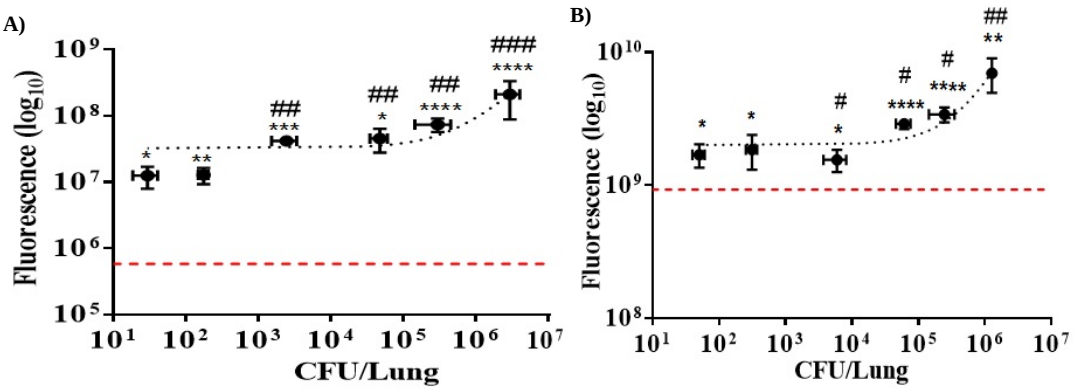

Figure 38: Fluorescence detected using whole-body imaging using intravital fiber excitation versus grouped CFU from lung homogenates for animals infected with (A) tdTomato-expressing *M. bovis* BCG and (B) *M. bovis* BCG labeled with REF substrate CNIR800. Bars represent average fluorescence of each group and error bars denote standard error. *p < 0.05, **p < 0.01, ***p < 0.001, ****p < 0.0001: significantly different as compared to the fluorescence in uninfected group, calculated by Student's two-tailed t-test. #p < 0.05, ##p < 0.01, ###p < 0.001: significantly different as compared to the fluorescence in uninfected group, calculated by Kruskal-Wallis for multiple comparisons with the Bonferroni posttest.

6.4 Conclusions

We integrated a fiber optic fluorescence microendoscope into a whole-body imaging system for detection of pulmonary infection in-vivo using a NIR BlaC-specific fluorogenic substrate. We determined optimal methods for achieving the best SNR, including imaging time after fluorogenic substrate administration and the position of the animal during imaging. We demonstrated that integration of these optical imaging technologies with BlaC-specific fluorescent reporter probes enables sensitive detection of bacteria in lungs of living animals down to ~100 CFU (using Student's t-test), an improvement of two orders of magnitude over whole-body epi-illumination. This technology can also improve the sensitivity of whole-body optical imaging to enable study of early stage bacterial infection, evaluation of therapeutic efficacy, and development of preventative treatments.

These studies are consistent with previous reports showing significant improvement of detection sensitivity using intravital excitation to detect tdTomato-expressing *M. bovis* BCG in the lungs of live animals [124]. The greater improvement of intravital excitation with tdTomato in comparison to CNIR800 can be attributed to the shorter excitation wavelength of tdTomato and higher absorption of that wavelength by tissue. The use of CNIR800 allows application to native strains of Mtb and the potential for clinical translation. Our results also demonstrate improvement of detection threshold for REF imaging in live animals compared to both epi-illumination and trans-illumination.

CHAPTER VII

CONCLUSION AND FUTURE WORK

7.1 Major contributions of this dissertation

We developed an intravital fluorescence microendoscope to detect and quantify respiratory bacterial infection, specifically tuberculosis, with high sensitivity. The developed imaging technique can be used to enhance study of bacterial pathogenesis in physiologically relevant infections, and enable rapid development of diagnostic and therapeutic techniques. The microendoscope was integrated to the IVIS whole-animal fluorescence imager to enable intravital excitation in the mouse lung with whole-animal detection, improve the sensitivity of the epi-illumination whole-animal imager and sensitively detect low numbers of bacteria in-vivo. Epi- and trans-illumination methods are limited in their ability to get sufficient excitation light into the animal for excitation of fluorescent targets deep inside the body. Therefore, by delivering the excitation light internally using the intravital microendoscope, the attenuation of the excitation light by tissue structures and skin is greatly decreased, allowing for increased delivery of excitation light to the region of interest.

We demonstrated the capabilities of the integrated imaging system using groups of animals infected by intratracheal instillation of 10^1–10^6 CFU BCG17 (tdTomato-expressing BCG strain) or 10^5 CFU BCG39 (same plasmid without tdTomato) as a vector control. Using this technique, the threshold of detection was measured as 10^3 CFU during

pulmonary infection (using non-parametric statistical test). Whereas, epi-illumination for whole-animal imaging was unable to detect infections, even with 10^6 CFU present.

We demonstrated that the integration of these optical imaging technologies with a BlaC-specific fluorescent probe, using REF technology, increased the system sensitivity to ~100 CFU (using parametric student's t-test). The low detection threshold enables the study of early stage bacterial infection and could allow for longitudinal studies of disease progression and therapeutic efficacy with multiple time points in a single animal. Also, one of the main advantages of REF technology is that no recombinant strain is needed, enabling clinical translation of the technology.

7.2 Future work

7.2.1 Evaluate therapeutic and vaccine efficacy in animal models

Having established the ability of the intravital fiber-based microendoscope integrated to IVIS whole-animal fluorescence imager to sensitively detect low number of bacteria in-vivo, the next step would be evaluation of therapeutic efficacy and development of preventative treatments using the developed imaging system. The ability of real-time detection of low numbers of bacteria in live animals, make this system suitable for study of early stage bacterial infection, and assessment of TB drugs and vaccines.

7.2.2 Modeling light transport in the mouse lung for enhanced optical detection of pulmonary tuberculosis and optimization of the imaging system

Because of the complex structure of lung tissue, the capabilities of the intravital excitation source and external detection are not well-defined. By modeling light transport

within the mouse lung and validating the model using optical phantoms, we could predict the behavior of the illumination light inside the body, which would facilitate optimizing the imaging system in order to improve the detection sensitivity.

7.2.3 Develop a fiber sensor to sensitively detect the REF fluorescence reporter in-vivo

Based on the capability of the intravital microendoscope to detect fluorescence signal, which is independent from IVIS signal detection, a fiber sensor can be designed for use in the development of therapeutics and vaccines without the need of the whole-animal imaging system.

REFERENCES

1. World Health Organization; *Global Tuberculosis report;* 2014.
2. Tsara, V., E. Serasli, and P. Christaki, *Problems in diagnosis and treatment of tuberculosis infection.* Hippokratia, 2009. **13**(1): p. 20.
3. Crosta, P., *"What is Tuberculosis? What causes Tuberculosis?."*, Medical News Today. 2009.
4. Flynn, J.L. and J. Chan, *Tuberculosis: latency and reactivation.* Infection and Immunity, 2001. **69**(7): p. 4195-4201.
5. Selwyn, P.A., D. Hartel, V. A. Lewis, E. E. Schoenbaum, S. H. Vermund, et al., *A prospective study of the risk of tuberculosis among intravenous drug users with human immunodeficiency virus infection.* New England Journal of Medicine, 1989. **320**(9): p. 545-550.
6. Sasindran, S.J. and J.B. Torrelles, *Mycobacterium tuberculosis infection and inflammation: what is beneficial for the host and for the bacterium.* Front Microbiol, 2011. **2**(2): p. 2.
7. Kim, H.R., S. S. Hwang, H. J. Kim, S. M. Lee, C. G. Yoo, et al., *Impact of extensive drug resistance on treatment outcomes in non-HIV-infected patients with multidrug-resistant Tuberculosis.* Clinical Infectious Diseases, 2007. **45**(10): p. 1290-1295.
8. Zhao, M., X. Li, P. Xu, X. Shen, X. Gui, et al., *Transmission of MDR and XDR Tuberculosis in Shanghai, China.* PLoS ONE, 2009. **4**(2): p. e4370.

9. Comstock, G.W., *Efficacy of BCG vaccine.* Journal of the American Medical Association, 1994. **272**(10): p. 766-766.

10. Fine, P. and L. Rodrigues, *Mycobacterial diseases.* The Lancet, 1990. **335**(8696): p. 1016-1020.

11. Lalvani, A., *Diagnosing tuberculosis infection in the 21st century: new tools to tackle an old enemy.* Chest, 2007. **131**(6): p. 1898-906.

12. *TB Testing & Diagnosis*. 2014; Available from: www.cdc.gov/tb/topic/testing/.

13. Steingart, K.R., M. Henry, V. Ng, P. C. Hopewell, A. Ramsay, et al., *Fluorescence versus conventional sputum smear microscopy for tuberculosis: a systematic review.* The Lancet Infectious Diseases, 2006. **6**(9): p. 570-581.

14. Lumb, R., A. Van Deun, I. Bastian, and M. Fitz-Gerald, *Laboratory diagnosis of tuberculosis by sputum microscopy: The Handbook.* Pacific Island Countries, Adelaide, Australia, 2013.

15. Thomsen, V.O., A. Kok-Jensen, M. Buser, S. Philippi-Schulz, and H.-J. Burkardt, *Monitoring treatment of patients with pulmonary tuberculosis: can PCR be applied?,* Journal of Clinical Microbiology, 1999. **37**(11): p. 3601-3607.

16. Chalfie, M., Y. Tu, G. Euskirchen, W.W. Ward, and D.C. Prasher, *Green fluorescent protein as a marker for gene expression.* Science, 1994. **263**(5148): p. 802-805.

17. Shaner, N.C., P.A. Steinbach, and R.Y. Tsien, *A guide to choosing fluorescent proteins.* Nature Methods, 2005. **2**(12): p. 905-909.

18. Andreu, N., A. Zelmer, and S. Wiles, *Noninvasive biophotonic imaging for studies of infectious disease.* FEMS Microbiology Reviews, 2011. **35**(2): p. 360-394.

19. Zonios, G., J. Bykowski, and N. Kollias, *Skin melanin, hemoglobin, and light scattering properties can be quantitatively assessed in vivo using diffuse reflectance spectroscopy.* Journal of Investigative Dermatology, 2001. **117**(6): p. 1452-1457.

20. Jabbour, J.M., M.A. Saldua, J.N. Bixler, and K.C. Maitland, *Confocal endomicroscopy: instrumentation and medical applications.* Annals of Biomedical Engineering, 2012. **40**(2): p. 378-397.

21. Kaijzel, E.L., G. Kaijzel, C.W.G.M. van der Pluijm, and Lowik, *Whole-body optical imaging in animal models to assess cancer development and progression.* Clinical Cancer Research, 2007. **13**(12): p. 3490-3497.

22. Kong, Y., A. R. Akin, K. P. Francis, N. Zhang, T. L. Troy, et al., *Whole-body imaging of infection using fluorescence*, Current Protocols in Microbiology. 2011, p; 2C-3.

23. Francis, K.P., J. Yu, C. Bellinger-Kawahara, D. Joh, M. J. Hawkinson, et al., *Visualizing pneumococcal infections in the lungs of live mice using bioluminescent streptococcus pneumoniae transformed with a novel gram-positive lux transposon.* Infection and Immunity, 2001. **69**(5): p. 3350-3358.

24. Rocchetta, H., C. J. Boylan, J. W. Foley, P. W. Iversen, D. L. LeTourneau, et al., *Validation of a noninvasive, real-time imaging technology using bioluminescent*

Escherichia coli in the neutropenic mouse thigh model of infection. Antimicrobial Agents and Chemotherapy, 2001. **45**(1): p. 129-137.

25. Kadurugamuwa, J.L., K. Modi, J. Yu, K. P. Francis, C. Orihuela, et al., *Noninvasive monitoring of pneumococcal meningitis and evaluation of treatment efficacy in an experimental mouse model.* Molecular Imaging, 2005. **4**(2): p. 137.
26. Contag, C.H., P. R. Contag, J. I. Mullins, S. D. Spilman, D. K. Stevenson, et al., *Photonic detection of bacterial pathogens in living hosts.* Molecular Microbiology, 1995. **18**(4): p. 593-603.
27. Rice, B.W., M.D. Cable, and M.B. Nelson, *In vivo imaging of light-emitting probes.* Journal of Biomedical Optics, 2001. **6**(4): p. 432-440.
28. Troy, T., D. Jekic-McMullen, L. Sambucetti, and B. Rice, *Quantitative comparison of the sensitivity of detection of fluorescent and bioluminescent reporters in animal models.* Molecular Imaging, 2004(3): p. 9-23.
29. Inoue, Y., K. Izawa, S. Kiryu, A. Tojo, and K. Ohtomo, *Diet and abdominal autofluorescence detected by in vivo fluorescence imaging of living mice.* Molecular Imaging, 2008. **7**(1): p. 21-27.
30. Xu, H. and B.W. Rice, *In-vivo fluorescence imaging with a multivariate curve resolution spectral unmixing technique.* Journal of Biomedical Optics, 2009. **14**(6): p. 064011-064011-9.
31. Mufti, N., Y. Mufti, J. Kong, K. Cirillo, and Maitland, *Fiber optic microendoscopy for preclinical study of bacterial infection dynamics.* Biomedical Optics Express, 2011. **2**(5): p. 1121.

32. Ntziachristos, V., *Fluorescence molecular imaging.* Annual Review Of Biomedical Engineering, 2006. **8**: p. 1-33.

33. Jain, R.K., L.L. Munn, and D. Fukumura, *Dissecting tumour pathophysiology using intravital microscopy.* Nature Reviews Cancer, 2002. **2**(4): p. 266-276.

34. Ragan, T.M., H. Huang, and P.T. So, *In vivo and ex vivo tissue applications of two-photon microscopy.* Methods in Enzymology, 2002. **361**: p. 481-505.

35. Condeelis, J. and J.E. Segall, *Intravital imaging of cell movement in tumours.* Nature Reviews Cancer, 2003. **3**(12): p. 921-930.

36. Vooijs, M., J. Jonkers, S. Lyons, and A. Berns, *Noninvasive imaging of spontaneous retinoblastoma pathway-dependent tumors in mice.* Cancer Research, 2002. **62**(6): p. 1862-1867.

37. Yang, M., E. Baranov, P. Jiang, F. Sun, X. Li, et al., *Whole-body optical imaging of green fluorescent protein-expressing tumors and metastases.* Proceedings of the National Academy of Sciences, 2000. **97**(3): p. 1206-1211.

38. Zhong, W., J. P. Celli, I. Rizvi, Z. Mai, B. Q. Spring, et al., *In vivo high-resolution fluorescence microendoscopy for ovarian cancer detection and treatment monitoring.* British Journal of Cancer, 2009. **101**(12): p. 2015-2022.

39. Yang, M. and Yang, *Whole-body and intravital optical imaging of angiogenesis in orthotopically implanted tumors.* Proceedings of the National Academy of Sciences of the United States of America, 2001. **98**(5): p. 2616-2621.

40. Kong, Y., S. Subbian, S.L.G. Cirillo, and J.D. Cirillo, *Application of optical imaging to study of extrapulmonary spread by tuberculosis.* Tuberculosis, 2009. **89, Supplement 1**(0): p. S15-S17.

41. Leblond, F., S.C. Davis, P.A. Valdés, and B.W. Pogue, *Pre-clinical whole-body fluorescence imaging: Review of instruments, methods and applications.* Journal of Photochemistry and Photobiology B: Biology, 2010. **98**(1): p. 77-94.

42. Wiles, S., K.M. Pickard, K. Peng, T.T. MacDonald, and G. Frankel, *In vivo bioluminescence imaging of the murine pathogen Citrobacter rodentium.* Infection and Immunity, 2006. **74**(9): p. 5391-5396.

43. Kuklin, N.A., G. D. Pancari, T. W. Tobery, L. Cope, J. Jackson, et al., *Real-time monitoring of bacterial infection in vivo: development of bioluminescent staphylococcal foreign-body and deep-thigh-wound mouse infection models.* Antimicrobial Agents and Chemotherapy, 2003. **47**(9): p. 2740-2748.

44. Kong, Y., H. Yao, H. Ren, S. Subbian, S. L. G. Cirillo, et al., *Imaging tuberculosis with endogenous β-lactamase reporter enzyme fluorescence in live mice.* Proceedings of the National Academy of Sciences, 2010. **107**(27): p. 12239-12244.

45. Gmitro, A.F. and D. Aziz, *Confocal microscopy through a fiber-optic imaging bundle.* Optics Letters, 1993. **18**(8): p. 565-567.

46. Knittel, J., L. Schnieder, G. Buess, B. Messerschmidt, and T. Possner, *Endoscope-compatible confocal microscope using a gradient index-lens system.* Optics Communications, 2001. **188**(5): p. 267-273.

47. Sung, K.-B., R. R. Kortum, M. Follen, A. Malpica, C. Liang, et al., *Fiber optic confocal reflectance microscopy: a new real-time technique to view nuclear morphology in cervical squamous epithelium in vivo.* Optics Express, 2003. **11**(24): p. 3171-3181.

48. Mark, P., Y. Dihua, R. R. Kortum, *High-resolution fiber-optic microendoscopy for in situ cellular imaging.* Journal of Visualized Experiments, 2011(47): pp. e2306-e2306.

49. Muldoon, T.J., *Subcellular-resolution molecular imaging within living tissue by fiber microendoscopy.* Optics Express, 2007. **15**(25): p. 16413.

50. Sun, J., C. Sun, B. Shu, R. Appiah, and Drezek, *Needle-compatible single fiber bundle image guide reflectance endoscope.* Journal of Biomedical Optics, 2010. **15**(4): p. 040502.

51. Vila, P., C.W. Park, M. C. Pierce, G. H. Goldstein, L. Levy, et al., *Discrimination of Benign and Neoplastic Mucosa with a High-Resolution Microendoscope (HRME) in Head and Neck Cancer.* Annals of Surgical Oncology, 2012. **19**(11): p. 3534-3539.

52. Muldoon, T.J., S. Anandasabapathy, D. Maru, and R. Richards-Kortum, *High-resolution imaging in Barrett's esophagus: a novel, low-cost endoscopic microscope.* Gastrointestinal Endoscopy, 2008. **68**(4): p. 737-744.

53. Ligler, F.S., K. E. Sapsford, J. P. Golden, L. C. Shriver-Lake, C. R. Taitt, et al., *The array biosensor: portable, automated systems.* Analytical Sciences, 2007. **23**(1): p. 5-10.

54. Geng, T., J. Uknalis, S.-I. Tu, and A.K. Bhunia, *Fiber-optic biosensor employing Alexa-Fluor conjugated antibody for detection of Escherichia coli O157: H7 from ground beef in four hours.* Sensors, 2006. **6**(8): p. 796-807.

55. Ahmed, A., J.V. Rushworth, N.A. Hirst, and P.A. Millner, *Biosensors for whole-cell bacterial detection.* Clinical Microbiology Reviews, 2014. **27**(3): p. 631-646.

56. Taniguchi, M., E. Akai, T. Koshida, K. Hibi, H. Kudo, et al. *A fiber optic immunosensor for rapid bacteria determination*. 3rd Kuala Lumpur International Conference on Biomedical Engineering, 2007, pp. 308-311.

57. Zhu, C., Q. Liu, and N. Ramanujam, *Effect of fiber optic probe geometry on depth-resolved fluorescence measurements from epithelial tissues: a Monte Carlo simulation.* Journal of Biomedical Optics, 2003. **8**(2): p. 237-247.

58. Elahi, S.F., *Assessing molecular biomarkers in living mice using fluorescence microendoscopy and spectroscopy*. PhD diss., The University of Michigan, 2014.

59. Ordway, D.J. and I.M. Orme, *Animal models of mycobacteria infection.* Current Protocols in Immunology, 2011: p. 19.5. 1-19.5. 50.

60. Sande, M.A., *Handbook of animal models of infection: experimental models in antimicrobial chemotherapy*. 1999: Academic Press.

61. Basaraba, R.J., *Experimental tuberculosis: the role of comparative pathology in the discovery of improved tuberculosis treatment strategies.* Tuberculosis, 2008. **88**: p. S35-S47.

62. Shimizu, S., *Routes of administration.* The laboratory Mouse, 2004: p. 527-541.

63. Kiessling, F., J. Pichler, and P. Hauff, *Small animal imaging*, Springer, Berlin Heidelberg, 2011.

64. Small, W., P. R. Buckley, T. S. Wilson, J. M. Loge, K. D. Maitland, et al., *Fabrication and characterization of cylindrical light diffusers comprised of shape memory polymer.* Journal of Biomedical Optics, 2008. **13**(2): p. 024018-024018-7.

65. Xu, H. and B. Rice, *Spectral unmixing for in-vivo imaging*. 2007, Google Patents.

66. Hu, Y.H., H. Lee, and F. Scarpace, *Optimal linear spectral unmixing.* Geoscience and Remote Sensing, IEEE Transactions on Geoscience and Remote Sensing, 1999. **37**(1): p. 639-644.

67. Sciences, C.L., *Living Image® Software User's Manual*. 2012, Caliper Corporation: Massachusetts, USA.

68. Yuste, R., *Fluorescence microscopy today.* Nature Methods, 2005. **2**(12): p. 902-904.

69. Baker, M., *Whole-animal imaging: The whole picture.* Nature, 2010. **463**(7283): p. 977-980.

70. Billinton, N. and A.W. Knight, *Seeing the wood through the trees: a review of techniques for distinguishing green fluorescent protein from endogenous autofluorescence.* Analytical Biochemistry, 2001. **291**(2): p. 175-197.

71. Wagnieres, G.A., W.M. Star, and B.C. Wilson, *In vivo fluorescence spectroscopy and imaging for oncological applications.* Photochemistry and Photobiology, 1998. **68**(5): p. 603-632.

72. Ntziachristos, V., C.-H. Tung, C. Bremer, and R. Weissleder, *Fluorescence molecular tomography resolves protease activity in vivo.* Nature Medicine, 2002. **8**(7): p. 757-761.

73. Tamgüney, G., K. P. Francis, K. Giles, A. Lemus, S. J. DeArmond, et al., *Measuring prions by bioluminescence imaging.* Proceedings of the National Academy of Sciences, 2009. **106**(35): p. 15002-15006.

74. Chen, J., *In vivo imaging of proteolytic activity in atherosclerosis.* Circulation, 2002. **105**(23): p. 2766-2771.

75. Sosnovik, D.E., *Fluorescence tomography and magnetic resonance imaging of myocardial macrophage infiltration in infarcted myocardium in vivo.* Circulation, 2007. **115**(11): p. 1384-1391.

76. Flusberg, B.A., E. D. Cocker, W. Piyawattanametha, J. C. Jung, E. L. M. Cheung, et al., *Fiber-optic fluorescence imaging.* Nature Methods, 2005. **2**(12): p. 941-950.

77. Oh, G., E. Chung, and S.H. Yun, *Optical fibers for high-resolution in vivo microendoscopic fluorescence imaging.* Optical Fiber Technology, 2013. **19**(6): p. 760-771.

78. Miller, S.J., C. M. Lee, B. P. Joshi, A. Gaustad, E. J. Seibel, et al., *Targeted detection of murine colonic dysplasia in vivo with flexible multispectral scanning*

fiber endoscopy. Journal of Biomedical Optics, 2012. **17**(2): p. 0211031-02110311.

79. Choi, Y., C. Yoon, M. Kim, T. D. Yang, C. Fang-Yen, et al., *Scanner-free and wide-field endoscopic imaging by using a single multimode optical fiber.* Physical Review Letters, 2012. **109**(20): p. 203901.

80. Lee, C.M., C.J. Engelbrecht, T.D. Soper, F. Helmchen, and E.J. Seibel, *Scanning fiber endoscopy with highly flexible, 1 mm catheterscopes for wide-field, full-color imaging.* Journal of Biophotonics, 2010. **3**(5-6): p. 385-407.

81. Zhang, Y., *A compact fiber-optic SHG scanning endomicroscope and its application to visualize cervical remodeling during pregnancy.* Proceedings of the National Academy of Sciences, 2012. **109**(32): p. 12878-12883.

82. Bao, H., A. Boussioutas, R. Jeremy, S. Russell, and M. Gu, *Second harmonic generation imaging via nonlinear endomicroscopy.* Optics Express, 2010. **18**(2): p. 1255-1260.

83. Brown, C.M., *In vivo imaging of unstained tissues using a compact and flexible multiphoton microendoscope.* Journal of Biomedical Optics, 2012. **17**(4): p. 0405051-0405053.

84. Keahey, P., T. Tkaczyk, K. Schmeler, and R. Richards-Kortum, *Optimizing modulation frequency for structured illumination in a fiber-optic microendoscope to image nuclear morphometry in columnar epithelium.* Biomedical Optics Express, 2015. **6**(3): p. 870-880.

85. Iftimia, N., *Fluorescence-guided optical coherence tomography imaging for colon cancer screening: a preliminary mouse study.* Biomedical Optics Express, 2012. **3**(1): p. 178-191.

86. Lorenser, D., *Dual-modality needle probe for combined fluorescence imaging and three-dimensional optical coherence tomography.* Optics Letters, 2013. **38**(3): p. 266-268.

87. Cheng, S., *Flexible endoscope for continuous in vivo multispectral fluorescence lifetime imaging.* Optics Letters, 2013. **38**(9): p. 1515-1517.

88. Pierce, M., D. Yu, and R. Richards-Kortum, *High-resolution fiber-optic microendoscopy for in situ cellular imaging.* Journal of Visualized Experiments, 2011(47): p. e2306.

89. Gordon, S., S. Keshav, and M. Stein, *BCG-induced granuloma formation in murine tissues.* Immunobiology, 1994. **191**(4): p. 369-377.

90. Kong, Y., A.R. Akin, K. P. Francis, N. Zhang, T. L. Troy, et al., *Whole-body imaging of infection using fluorescence.* Current Protocols in Microbiology, 2011: p. 2C. 3.1-2C. 3.21.

91. Mufti, N., Y. Kong, J.D. Cirillo, and K.C. Maitland, *Fiber optic microendoscopy for preclinical study of bacterial infection dynamics.* Biomedical Optics Express, 2011. **2**(5): p. 1121-1134.

92. Goldgeier, M., C.A. Fox, J.M. Zavislan, D. Harris, and S. Gonzalez, *Noninvasive imaging, treatment, and microscopic confirmation of clearance of basal cell carcinoma.* Dermatologic Surgery, 2003. **29**(3): p. 205-210.

93. Shaner, N.C., *Improving the photostability of bright monomeric orange and red fluorescent proteins.* Nature Methods, 2008. **5**(6): p. 545-551.

94. Gee, J.M., N.A. Smith, F. R. Fernandez, M. N. Economo, D. Brunert, et al., *Imaging activity in neurons and glia with a Polr2a-based and cre-dependent GCaMP5G-IRES-tdTomato reporter mouse.* Neuron, 2014. **83**(5): p. 1058-1072.

95. Dedecker, P., G.C. Mo, T. Dertinger, and J. Zhang, *Widely accessible method for superresolution fluorescence imaging of living systems.* Proceedings of the National Academy of Sciences, 2012. **109**(27): p. 10909-10914.

96. Chudakov, D.M., M.V. Matz, S. Lukyanov, and K.A. Lukyanov, *Fluorescent proteins and their applications in imaging living cells and tissues.* Physiological Reviews, 2010. **90**(3): p. 1103-1163.

97. Capoulade, J., M. Wachsmuth, L. Hufnagel, and M. Knop, *Quantitative fluorescence imaging of protein diffusion and interaction in living cells.* Nature Biotechnology, 2011. **29**(9): p. 835-839.

98. Sevick-Muraca, E., *Translation of near-infrared fluorescence imaging technologies: emerging clinical applications.* Annual Review of Medicine, 2012. **63**: p. 217-231.

99. Bird-Lieberman, E.L., *Molecular imaging using fluorescent lectins permits rapid endoscopic identification of dysplasia in Barrett's esophagus.* Nature Medicine, 2012. **18**(2): p. 315-321.

100. White, A.G., N. Fu, W. M.Leevy, J. Lee, M. A. Blasco, et al., *Optical imaging of bacterial infection in living mice using deep-red fluorescent squaraine rotaxane probes.* Bioconjugate Chemistry, 2010. **21**(7): p. 1297-1304.

101. MacLaurin, S.A., *Reduction of skin and food autofluorescence in different mouse strains through diet changes*. Society for Molecular Imaging, Annual Meeting, Hawaii. 2006.

102. Bhaumik, S., J. DePuy, and J. Klimash, *Strategies to minimize background autofluorescence in live mice during noninvasive fluorescence optical imaging.* Lab Animal, 2007. **36**(8): p. 40-43.

103. Muldoon, T.J., *Subcellular-resolution molecular imaging within living tissue by fiber microendoscopy.* Optics Express, 2007. **15**(25): p. 16413-16423.

104. Chang, M.H., S.L.G. Cirillo, and J.D. Cirillo, *Using luciferase to image bacterial infections in mice.* Journal of Visualized Experiments, 2011(48): p. e2547.

105. Dunnett, C.W., *A multiple comparison procedure for comparing several treatments with a control.* Journal of the American Statistical Association, 1955. **50**(272): p. 1096-1121.

106. Demšar, J., *Statistical comparisons of classifiers over multiple data sets.* The Journal of Machine Learning Research, 2006. **7**: p. 1-30.

107. García, S., A. Fernández, J. Luengo, and F. Herrera, *Advanced nonparametric tests for multiple comparisons in the design of experiments in computational intelligence and data mining: Experimental analysis of power.* Information Sciences, 2010. **180**(10): p. 2044-2064.

108. Travis, L.W., R.L. Hybels, and M. Newman, *Tuberculosis of the larynx.* The Laryngoscope, 1976. **86**(4): p. 549-558.

109. Gupta, P., S.V. Kolluri, B. Chandramouli, N. Venkataramana, and B. Das, *Calvarial tuberculosis: a report of two cases.* Neurosurgery, 1989. **25**(5): p. 830-833.

110. Bernaerts, A., F. M. Vanhoenacker, P. M. Parizel, J. W. M. Van Goethem, R. Van Altena, et al., *Tuberculosis of the central nervous system: overview of neuroradiological findings.* European radiology, 2003. **13**(8): p. 1876-1890.

111. Torres, R. M. and M. Calonge, *Macular edema as the only ocular finding of tuberculosis.* American Journal of Ophthalmology, 2004. **138**(6): p. 1048-1049.

112. Heuts, F., B. Carow, H. Wigzell, and M.E. Rottenberg, *Use of non-invasive bioluminescent imaging to assess mycobacterial dissemination in mice, treatment with bactericidal drugs and protective immunity.* Microbes and Infection, 2009. **11**(14): p. 1114-1121.

113. Hickey, M.J., et al., *Luciferase in vivo expression technology: use of recombinant mycobacterial reporter strains to evaluate antimycobacterial activity in mice.* Antimicrobial Agents and Chemotherapy, 1996. **40**(2): p. 400-407.

114. Arain, T.M., A.E. Resconi, M.J. Hickey, and C.K. Stover, *Bioluminescence screening in vitro (Bio-Siv) assays for high-volume antimycobacterial drug discovery.* Antimicrobial Agents and Chemotherapy, 1996. **40**(6): p. 1536-1541.

115. Andrew, P.W. and I. Roberts, *Construction of a bioluminescent mycobacterium and its use for assay of antimycobacterial agents.* Journal of Clinical Microbiology, 1993. **31**(9): p. 2251-2254.

116. Cooksey, R., J. Crawford, W. Jacobs, and T. Shinnick, *A rapid method for screening antimicrobial agents for activities against a strain of Mycobacterium tuberculosis expressing firefly luciferase.* Antimicrobial Agents and Chemotherapy, 1993. **37**(6): p. 1348-1352.

117. Davis, S. L., A. Be Nicholas, G. Lamichhane, S. Nimmagadda, M. G. Pomper, et al., *Bacterial thymidine kinase as a non-invasive imaging reporter for Mycobacterium tuberculosis in live animals.* PloS One, 2009. **4**(7): p. e6297.

118. Davis, S.L., E. L. Nuermberger, P. K. Um, C. Vidal, B. Jedynak, et al., *Noninvasive pulmonary [18F]-2-fluoro-deoxy-D-glucose positron emission tomography correlates with bactericidal activity of tuberculosis drug treatment.* Antimicrobial Agents and Chemotherapy, 2009. **53**(11): p. 4879-4884.

119. Wendland, M. and D. Bumann, *Optimization of GFP levels for analyzing Salmonella gene expression during an infection.* Federation of European Biochemical Societies Letters, 2002. **521**(1): p. 105-108.

120. Rang, C., J.E. Galen, J.B. Kaper, and L. Chao, *Fitness cost of the green fluorescent protein in gastrointestinal bacteria.* Canadian Journal of Microbiology, 2003. **49**(9): p. 531-537.

121. Coulson, N.M., M. Fulop, and R.W. Titball, *Effect of different plasmids on colonization of mouse tissues by the aromatic amino acid dependent Salmonella typhimurium SL 3261.* Microbial Pathogenesis, 1994. **16**(4): p. 305-311.

122. Xing, B., A. Khanamiryan, and J. Rao, *Cell-permeable near-infrared fluorogenic substrates for imaging β-lactamase activity.* Journal of the American Chemical Society, 2005. **127**(12): p. 4158-4159.

123. Kong, Y. and J. D. Cirillo, *Reporter enzyme fluorescence (REF) imaging and quantification of tuberculosis in live animals.* Virulence, 2010. **1**(6): p. 558-562.

124. Nooshabadi, F., H. J. Yang, J. N. Bixler, Y. Kong, J. D. Cirillo, et al., *Intravital Fluorescence Excitation in Whole-Animal Optical Imaging.* PLoS ONE, 2016. **11**(2): p. e0149932.